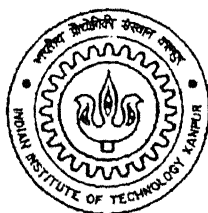


**EXPERIMENTAL GAMMA-RAY  
TOMOGRAPHY  
WITH LIMITED DATA**

*by*

**PRANAV KUMAR VARSHNEY**



**NETP  
1997**

*to the*

**NUCLEAR ENGINEERING & TECHNOLOGY PROGRAMME  
INDIAN INSTITUTE OF TECHNOLOGY  
KANPUR**

December, 1997

**M  
VAR  
EXP**

# **EXPERIMENTAL GAMMA-RAY TOMOGRAPHY WITH LIMITED DATA**

A Thesis Submitted  
in Partial Fulfillment of the Requirements  
for the Degree of

**MASTER OF TECHNOLOGY**

*by*

**PRANAV KUMAR VARSHNEY**



*to the*

**NUCLEAR ENGINEERING & TECHNOLOGY PROGRAMME  
INDIAN INSTITUTE OF TECHNOLOGY  
KANPUR**

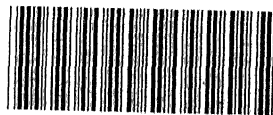
December, 1997

55 MAR 1998 / NETP  
CENTRAL LIBRARY  
1.1 125020  
Iss. No. A

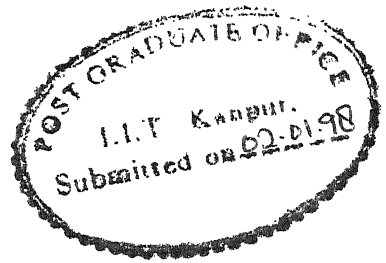
NETP-1997-M-VAR-EXP

Entered in System

Nov 8 49  
6-4-98

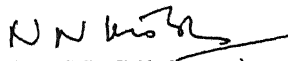



A125020



# Certificate

Certified that the work contained in the thesis entitled "**EXPERIMENTAL GAMMA-RAY TOMOGRAPHY WITH LIMITED DATA**", by **Pranav Kumar Varshney**, has been carried out under our supervision and that this work has not been submitted elsewhere for a degree.

  
(Dr. N. N. Kishore)  
Professor  
Department of Mechanical  
Engineering,  
Indian Institute of Technology,  
Kanpur.

  
(Dr. P. Munshi)  
Professor  
Department of Mechanical  
Engineering & Nuclear Engineering  
Technology Programme,  
Indian Institute of Technology,  
Kanpur.

*DEDICATED TO  
MY  
BELOVED PARENTS*

# Acknowledgements

*With profound sense of gratitude, I take this opportunity to thank Dr. P. Munshi and Dr. N. N. Kishore for introducing me to the CT and giving me the chance to work in this field. It was their kind concern, constant encouragement and valuable guidance which led to the completion of this work.*

*I am grateful to all faculty members, specially Dr. M. S. Kalra, Dr. K. S. Ram, who taught me various courses during my M. Tech. programme.*

*A special note of thanks is due to Debasis and Satya for their substantial and effective help in this work.*

*I wish to thank all the staff members of NET department for their valuable co-operation.*

*Finally, I would like to thank my friends at Hall-4, specially Gaurav, Surendra, Suresh, Arvind, Navneet, the NET friends, who made my stay at IIT Kanpur, comfortable and enjoyable.*

**Pranav Kumar Varshney**

# Abstract

The technique of computerized tomography (CT) has established itself as a leading tool in diagnostic radiology over the past thirty years and is catching on fast in the non-destructive evaluation area in a variety of situations.

Image reconstruction from projections are based either on *transform methods* or *series expansion methods*. Series expansion methods made their first appearance in the scientific literature and in the CT scanner industry around 1970. Series expansion methods are used when limited amount of data is available. Series expansion methods include Algebraic Reconstruction Technique and other optimization methods. Algebraic Reconstruction Techniques can broadly classified in two groups, Additive Algebraic Reconstruction Techniques (ART) and Multiplicative Algebraic Reconstruction Techniques (MART).

Eight variations of ART and MART, are presented and compared in this work. Iterative tomographic algorithms have been applied to the reconstruction of simulated two-dimensional objects with internal defects. Comparison of the algorithms is based on their performance on the numerical generated objects. Impact of the variation of number of projections, projection angles, relaxation factor on the reconstructed images by these algorithms have been studied.

The study shows that of the eight reconstruction algorithms applicable in the limited-data situation, those based on MART are fastest, most flexible and most accurate. The best of the algorithms is applied to the reconstruction of real data from  $\gamma$ -ray scanner. This algorithm produces good reconstructions from limited amount of data. The data set includes projections at 4 angles over a  $180^\circ$  total angle of view ( $0^\circ, 45^\circ, 90^\circ, 135^\circ$ ).

# Contents

List of Figures	vi
List of Tables	viii
<b>1 INTRODUCTION</b>	<b>1</b>
1.1 Reconstruction from projections . . . . .	1
1.2 Reconstruction techniques . . . . .	2
1.3 Present work . . . . .	3
1.4 Thesis layout . . . . .	4
<b>2 THEORETICAL FORMULATION</b>	<b>5</b>
2.1 Formulation of a discretized model: . . . . .	5
2.2 CT using $\gamma$ -rays . . . . .	6
2.3 Series Expansion Methods . . . . .	7
2.3.1 ART . . . . .	7
2.3.2 MART . . . . .	12
2.4 Convergence criteria . . . . .	14
2.5 Error analysis . . . . .	14
<b>3 Experimental setup</b>	<b>16</b>
3.1 Equipments . . . . .	16



---

3.1.1	Scintillation detector . . . . .	16
3.1.2	Linear amplifier . . . . .	19
3.1.3	Voltage units . . . . .	19
3.1.4	Single channel analyzer (SCA) . . . . .	20
3.1.5	Timer . . . . .	20
3.1.6	Scalar . . . . .	20
3.2	Data collection . . . . .	20
3.3	Sources of error . . . . .	21
3.4	Precautions . . . . .	22
<b>4</b>	<b>Validation of Programs</b>	<b>23</b>
4.1	Simulated data . . . . .	23
4.2	Experimental data . . . . .	30
<b>5</b>	<b>Results</b>	<b>49</b>
5.1	Simulated data . . . . .	49
5.1.1	Performance of ART . . . . .	49
5.1.2	Performance of MART . . . . .	49
5.1.3	Effect of relaxation parameter on ART and MART . . .	50
5.1.4	Comparison between ART and MART . . . . .	50
5.2	Experimental data . . . . .	52
<b>6</b>	<b>Conclusions</b>	<b>54</b>
6.1	Suggestions for future work . . . . .	55
	<b>REFERENCES</b>	<b>56</b>

# List of Figures

2.1	Square pixels model for reconstruction from projection . . . . .	6
3.1	Experimental set-up . . . . .	18
4.1	CosGauss phantom . . . . .	24
4.2	Oscillating pattern of GBH . . . . .	26
4.3	Mayinger ART reconstruction of CosGauss phantom using case F	31
4.4	Gordon ART reconstruction of CosGauss phantom using case F	32
4.5	Gilbert ART reconstruction of CosGauss phantom using case F	32
4.6	Anderson ART reconstruction of CosGauss phantom using case F	33
4.7	GBH reconstruction of CosGauss phantom using case F . . . . .	33
4.8	GH reconstruction of CosGauss phantom using case F . . . . .	34
4.9	Lent reconstruction of CosGauss phantom using case F . . . . .	34
4.10	Lent2 reconstruction of CosGauss phantom using case F . . . . .	35
4.11	Gilbert ART reconstruction of CosGauss phantom using case C	35
4.12	Gilbert ART reconstruction of CosGauss phantom using case I .	36
4.13	Lent2 reconstruction of CosGauss phantom using case C . . . . .	36
4.14	Lent2 reconstruction of CosGauss phantom using case I . . . . .	37
4.15	Circular plate with circular hole . . . . .	37
4.16	Reconstruction of a circular plate with circular hole using (a) case C, (b) case F, (c) case I . . . . .	38

4.17 Square plate with five holes . . . . .	39
4.18 Reconstruction of square plate with five holes using (a) case C, (b) case F, (c) case I . . . . .	39
4.19 line plots of the 11 <sup>th</sup> rows . . . . .	40
4.20 line plots of the 26 <sup>th</sup> rows . . . . .	40
4.21 line plots of the 41 <sup>st</sup> rows . . . . .	41
4.22 line plots of the 11 <sup>th</sup> rows . . . . .	41
4.23 line plots of the 26 <sup>th</sup> rows . . . . .	42
4.24 line plots of the 41 <sup>st</sup> rows . . . . .	42
4.25 Square plate with two holes . . . . .	43
4.26 Reconstruction of square plate with two holes using (a) case C, (b) case F, (c) case I . . . . .	43
4.27 Square plate with five inclusions . . . . .	44
4.28 Reconstruction of square plate with five inclusions using (a) case C, (b) case F, (c) case I . . . . .	44
4.29 Reconstruction with 2 views . . . . .	45
4.30 Reconstruction with 4 views . . . . .	45
4.31 Reconstruction with 12 views . . . . .	45
4.32 Line plot of the 6 <sup>th</sup> row of the reconstructed field by 4 views . .	46
4.33 Line plot of the 12 <sup>th</sup> row of the reconstructed field by 4 views .	46
4.34 Line plot of the 18 <sup>th</sup> row of the reconstructed field by 4 views .	47
4.35 Line plot of the 6 <sup>th</sup> row of the reconstructed field by 12 views . .	47
4.36 Line plot of the 12 <sup>th</sup> row of the reconstructed field by 12 views . .	48
4.37 Line plot of the 18 <sup>th</sup> row of the reconstructed field by 12 views . .	48

# List of Tables

4.1	Imaging geometries . . . . .	25
4.2	Performance of ART for CosGauss phantom . . . . .	25
4.3	performance of MART for CosGauss phantom . . . . .	26
4.4	performance of GBH for CossGauss phantom . . . . .	26
4.5	Variation of errors with relaxation parameter for Gilbert ART .	27
4.6	Variation of errors with relaxation parameter for Lent2 . . . . .	27
4.7	Variation of iterations and CPU time of Gilbert ART . . . . .	28
4.8	Errors in Gilbert ART . . . . .	28
4.9	Variation of Iterations and CPU time with projections in Lent2	29
4.10	Errors in Lent2 . . . . .	30

# Nomenclature

$f_j$	Exact value of the $j^{th}$ pixel
$\tilde{f}_j$	Reconstructed field value of $j^{th}$ pixel
$W_{ij}$	weight function
$\phi_i$	exact projection of $i^{th}$ ray
$\tilde{\phi}_i$	approximate projection of $i^{th}$
$\lambda$	relaxation factor
e	stopping criteria
$\alpha_i$	correction coefficient
$\Delta\phi_i$	difference in exact and approximate projection of $i^{th}$ ray
C	correction term
k	iteration number
$W_{max}$	maximum value of weight
N	total number of pixels
M	total number of rays
$\bar{f}$	average of field values
a	average error
d	normalized RMS error
r	normalized absolute error
E	maximum error
$\zeta$	normalizing factor
N	Number of photon counts after passing through the material
$N_0$	Initial number of photon counts
$\mu(r, \phi)$	Attenuation coefficient

# Chapter 1

## INTRODUCTION

### 1.1 Reconstruction from projections

Computerized Tomography (CT) is widely used in a large number of scientific, medical and technical fields. Hounsfield, inventor of first CT scanner, shared Nobel prize with A. M. Cormack in 1979, for their pioneering achievement in the field of computerized tomography. Algorithms for the image reconstruction from projection have extended our ability to visualize the internal structures of objects in a broad spectrum of physical applications ranging from molecular dimensions (electron microscopy) to cosmic dimensions (radio astronomy). In words of *Herman*<sup>[1]</sup> :

”Image Reconstruction from projections is the process of producing an image of two-dimensional distribution (usually of some physical property) from estimates of its line integrals along a finite number of lines of known locations”.

In past, CT was done by X-rays but now other sources like  $\gamma$ -ray, acoustic, laser, microwave, neutrons, seismic, magnetic resonance, radar etc. are also used. X-ray dose reduction, speed up of scan time, or other practical limitations which restrict the range of angles of projections or the density of rays in certain projections, all may lead to incomplete projection data collection. Reconstruction from few directions arises in several nonmedical applications. With limited data, iterative methods generally perform better than other techniques. The iterative method converts the reconstruction problems

into a system of linear equations, with missing projection values treated like missing equations, i.e., they are ignored.

In  $\gamma$ -ray tomography, ray travels from source to receiver through the object. This ray contains the information of the part of object through which it passes. As the source and receiver are moved around the object, different projections are obtained. By these projections, the distribution of some physical property like attenuation coefficients within the object is reconstructed using one of the reconstruction techniques.

## 1.2 Reconstruction techniques

Reconstruction techniques are broadly classified in two group:

1. Transform methods or Direct methods.
2. Series expansion methods.

Direct methods include direct algebraic methods and Fourier Transform methods and Series expansion methods include *Algebraic Reconstruction Technique (ART)*, *Multiplicative Algebraic Technique (MART)*, *Simultaneous Iterative Reconstruction Technique (SIRT)*, *Entropy Optimization* etc. ART and MART are further classified into different classes depending upon the way corrections are applied to the algorithms.

The basic difference between the series expansion methods and the transform method is that in the former case the field to be reconstructed is discretized in the beginning, whereas in the later case continuous field is considered and at end the final formulas are discretized for computational purpose.

When the set of data available is large and complete, transform methods are generally used, whereas series expansion methods are preferred with incomplete data set. Series expansion methods are less efficient than transform methods (from computational speed and memory requirement point of view) but they can be used for irregular geometries.

Using these reconstruction techniques, some physical property of object

is calculated like attenuation coefficient or slowness (the inverse of acoustic velocity). In the ultrasonic tomography, the transit time from source to receiver is generally measured and then tomographic image which is a distribution of slowness is reconstructed. This is also known as *time-of-flight (TOF)* tomography.

### 1.3 Present work

In the present work, different series expansion methods, namely ART and MART are studied. These reconstruction techniques are applied on the simulated data, for the reconstruction of a two-dimensional field. *CosGauss phantom*, a numerically generated object, is used to compare various techniques in term of *CPU time*, *convergence rates* and *errors*. A situation in which the number of views is restricted but the total possible viewing angle is not, i.e. projections at five angles equally spaced over a  $180^\circ$  total angle of view, is used for comparison of reconstruction algorithms. The best algorithm among ART and the best among MART is then tested using a number of imaging geometries. The best among these two is further applied on various simulated two-dimensional fields which include Cosine phantom, circular plate with a central hole, square plate with five holes, square plate with two holes and square plate with five inclusions. This work has been carried out by Subbarao et al.<sup>[2]</sup> but here, the following differences exist:

- slightly different implementation of the algorithms,
- different errors measures are used,
- fewer number of rays are used, consistent with the  $\gamma$ -ray CT scanner on which real data have been taken.

Reconstruction is based on absorption coefficient data, as against simulated time-of-flight data used by Datta<sup>[3]</sup>.

The best reconstruction technique is then applied on real data, obtained by  $\gamma$ -ray CT scanner, to construct a two-dimensional field, which is the distribution



of absorption coefficient. Numerical computation were carried out on a DEC 400 workstation with 32 MB RAM and a 166 MHz processor.

## 1.4 Thesis layout

- Chapter 2 gives the detail of the reconstruction techniques, their algorithms and various error measures used for error analysis of these algorithms.
- Chapter 3 gives the detail of the experimental set-up used for scanning the specimen using the  $\gamma$ -ray CT scanner.
- Chapter 4 describes the application of the reconstruction techniques on the simulated fields. Different numerically generated fields used for testing the algorithms are discussed.
- Chapter 5 provides discussions on the results based on the simulated and real data.
- Chapter 6 summarizes the conclusions and suggests scope for further works.

# Chapter 2

## THEORETICAL FORMULATION

### 2.1 Formulation of a discretized model:

A cartesian grid of square picture elements, called pixel, is introduced into the region that has to be reconstructed. These pixels are numbered following a regular fashion as shown in fig. 2.1. The attenuation coefficient is assumed to be constant say  $x_j$  throughout the  $j^{th}$  pixel for  $j=1,2,..,N$ . Source and detector are considered as points and the rays between them as lines. The length of intersection of  $i^{th}$  ray with  $j^{th}$  pixel, denoted by  $W_{ij}$  for  $i=1,2,..,M$  and  $j=1,2,..,N$ , represents the contribution of  $j^{th}$  pixel to the total attenuation along the  $i^{th}$  ray.

The total attenuation of  $i^{th}$  ray, denoted by  $\phi_i$ , represents the line integral of the attenuation function along the path of ray. In this discretized model, the line integral takes the form of finite sum and the model may be described by a system of linear equations, as

$$\sum_{j=1}^N x_j W_{ij} = \phi_i \quad (2.1)$$

In matrix notation

$$\phi = \mathbf{W}\mathbf{X} \quad (2.2)$$

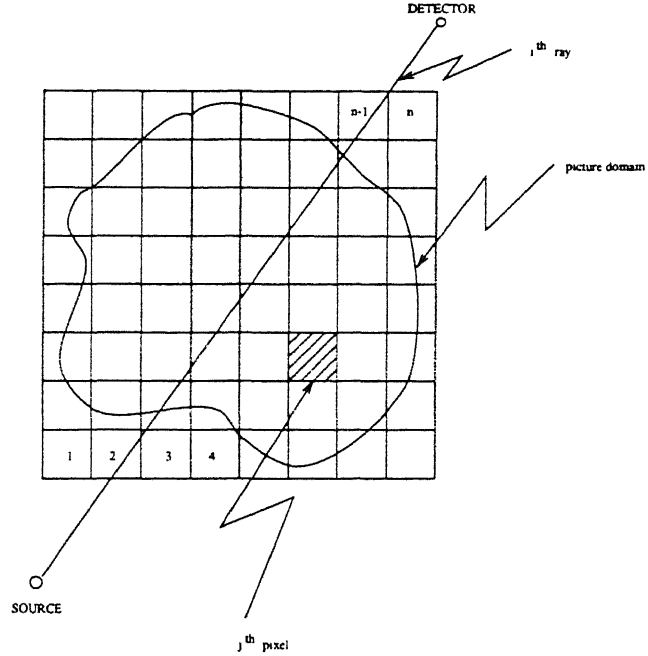


Figure 2.1: Square pixels model for reconstruction from projection

Problem now reduces to invert matrix  $W$ . The matrix  $W$  is quite sparse and its size may be large. Inversion of matrix  $W$  is quite impossible. Equation can be easily solved by series expansion methods. The goal of CT algorithms thus is to solve this set of  $M$  linear algebraic equations in  $N$  unknowns.

## 2.2 CT using $\gamma$ -rays

Following *Munshi*<sup>[4]</sup>, preliminary of  $\gamma$ -ray based CT is discussed below. Single beam mono-energetic radiation attenuation phenomenon in a plane can be represented by

$$N = N_0 \exp \left[ - \int_c \mu(r, \phi) \delta l \right] \quad (2.3)$$

The value of  $\mu$  is characteristic of a material for a given type of radiation and the energy of radiation. Equ. 2.3 considers  $\mu$  to be a two-dimensional function of position, as the path of radiation is assumed to be restricted to a plane. The energy dependence of  $\mu$  is also ignored. This is valid for  $\gamma$ -rays. Now, considering the material to have uniform attenuation coefficient,

equation 2.3 reduces to

$$N = N_0 \exp(-\mu \Delta l), \quad (2.4)$$

In general, any cross-section of interest will have non-uniform distribution. Rewriting equation 2.3 as

$$p = \int_c \mu(r, \phi) \delta l, \quad (2.5)$$

where,

$$p = \ln\left(\frac{N_0}{N}\right) \quad (2.6)$$

Now, to recover  $\mu$  we require several  $p$  values measured along various chord,  $c$ .

## 2.3 Series Expansion Methods

Different series expansion methods, namely ART and MART, are described in detail in the following subsections.

### 2.3.1 ART

Algebraic Reconstruction Technique (ART) was introduced by Gordon et al.<sup>[5]</sup> for solving the problem of three dimensional reconstruction from projections in electron microscopy and radiology and was later recognized to be identical with Kaczmarz's *algorithm*<sup>[6]</sup> for solving systems of linear equations. The first CT scanner developed by *Hounsfield*<sup>[7]</sup> used ART. Following *Censor*<sup>[8]</sup>, ART method used is presented below.

An iterative process starts from an initial approximation  $f^0 \in R^n$  to the image vector. In an iterative step, the current iterate  $f^k$  is corrected to a new iterate  $f^{k+1}$  by taking into account only a single ray, say  $i^{th}$ , and changing only the image values of the pixels which intersect this ray. The discrepancy between the measurement  $\phi_i$  and the pseudo-projection data  $\tilde{\phi}_i (= \sum_{j=1}^N W_{ij} f_j^k)$  obtained from the current image  $f^k$  is redistributed among the pixels along the  $i^{th}$  ray proportionally to their weights  $W_{ij}$  in the whole ray. In this way, the pixel values along the  $i^{th}$  ray are corrected to conform with the  $i^{th}$  measurement

without changing the rest of the image. Mathematically the whole process may be expressed as

$$f^{k+1} = f^k + \frac{\phi_i - \langle w^i, f^k \rangle}{\|w^i\|^2} w^i \quad (2.7)$$

where,

$$\langle w^i, f^k \rangle = \sum_{j=1}^N W_{ij} f_j^k \quad (2.8)$$

$$w^i = \sum_{j=1}^N W_{ij} \quad (2.9)$$

and

$$\|w^i\|^2 = \langle w^i, w^i \rangle \quad (2.10)$$

Introducing the relaxation parameter, the modified step for updating the iterate can be expressed as

$$f^{k+1} = f^k + \lambda \frac{\phi_i - \langle w^i, f^k \rangle}{\|w^i\|^2} w^i \quad (2.11)$$

where,  $\lambda$  is the relaxation parameter, which is the real number, usually confined to the interval

$$\epsilon_1 \leq \lambda \leq 2 - \epsilon_2, \quad \epsilon_1, \epsilon_2 > 0. \quad (2.12)$$

If the correction is negative, it may happen that the calculated field of a reconstructed image becomes negative, in which case it is set to zero, as discussed by *Gordon*<sup>[9]</sup>.

ART may be further classified in different categories depending upon the correction applied. The four forms of ART are mentioned below. For all these algorithms, let  $\tilde{f}_j$  for  $j=1,2,\dots,N$  be the initial approximation of field value or pixel value.

### 2.3.1.1 Mayinger ART

This is simplest iterative reconstruction algorithm proposed by *Mayinger*<sup>[10]</sup>. Pixel values are modified after all the correction values corresponding to the

individual rays are calculated. Let  $\phi_{i_\theta}$  be the projection due to  $i^{th}$  ray of view angle  $\theta$ . Algorithm for Mayinger ART is presented below.

For each view angle  $\theta$

Step 1: For each ray  $i_\theta$ , where  $i_\theta$  denotes  $i^{th}$  ray of view angle  $\theta$  and  $i_\theta$  varies from 1 to  $M_\theta$ , calculate

(a) The approximate projection ( $\tilde{\phi}_{i_\theta}$ ) as

$$\tilde{\phi}_{i_\theta} = \sum_{j=1}^N W_{i_\theta j} \tilde{f}_j \quad (2.13)$$

(b) Correction as

$$\Delta\phi_{i_\theta} = \phi_{i_\theta} - \tilde{\phi}_{i_\theta} \quad (2.14)$$

(c) Total value of weight function along each ray as

$$W_{i_\theta} = \sum_{j=1}^N W_{i_\theta j} \quad (2.15)$$

(d) Average value of correction as

$$\Delta\bar{\phi}_{i_\theta} = \frac{\Delta\phi_{i_\theta}}{W_{i_\theta}} \quad (2.16)$$

Step 2: Repeat step 1 for all rays of view angle  $\theta$ .

Step 3: For each ray  $i_\theta$ , modify the value of  $j^{th}$  pixel, for all  $j=1,2,\dots,N$ , as

$$\tilde{f}_j^k = \tilde{f}_j^{k-1} + \lambda \Delta\bar{\phi}_{i_\theta} \quad (2.17)$$

where  $\lambda$  denotes the relaxation factor.

Step 4: Repeat step 3 for all rays of view angle  $\theta$ .

Step 5: Repeat steps 1 to 4 for all view angles. This complete  $k^{th}$  iteration.

Step 6: Repeat steps 1 to 5 until

$$\frac{\tilde{f}^{k+1} - \tilde{f}^k}{\tilde{f}^k} \times 100 \leq e \quad (2.18)$$

where  $e$  is the stopping criteria.

### 2.3.1.2 Gordon ART

In this *method*<sup>[5]</sup> correction is applied to all pixels through which  $i^{th}$  ray passes, before correction for next ray is calculated. Thus, the number of rays in each view is not important. Algorithm is presented below.

For each iteration k

Step 1: For each ray i calculate

(a) The approximate projection ( $\tilde{\phi}_i$ ) as

$$\tilde{\phi}_i = \sum_{j=1}^N W_{ij} \tilde{f}_j \quad (2.19)$$

(b) Correction as

$$\Delta\phi_{i_g} = \phi_{i_g} - \tilde{\phi}_{i_g} \quad (2.20)$$

(c) Correction coefficient as

$$\alpha_i = \sum_{j=1}^N W_{ij}^2 \quad (2.21)$$

(d) Modify the value of  $j^{th}$  pixel, for all  $j=1,2,\dots,N$ , as

$$\tilde{f}_j^k = \tilde{f}_j^{k-1} + \frac{\lambda W_{ij} \Delta\phi_i}{\alpha_i} \quad (2.22)$$

where  $\lambda$  denotes the relaxation factor.

Step 2: Repeat steps (a) to (d) for all rays. This complete  $k^{th}$  iteration.

Step 3: Repeat steps 1 to 2 until

$$\frac{f^{k+1} - \tilde{f}^k}{\tilde{f}^k} \times 100 \leq e \quad (2.23)$$

where e is the stopping criteria.

### 2.3.1.3 Gilbert ART

This *algorithm*<sup>[11]</sup> is also called as simultaneous iterative reconstruction technique (SIRT). The pixel values are modified after all the correction values

corresponding to individual rays are calculated. Thus, it is similar to simple ART but correction applied to the pixel value is different from it. Algorithm is presented below.

For each iteration  $k$

Step 1: For each ray  $i$  calculate

(a) The approximate projection ( $\tilde{\phi}_i$ ) as

$$\tilde{\phi}_i = \sum_{j=1}^N W_{ij} \tilde{f}_j \quad (2.24)$$

(b) Correction as

$$\Delta\phi_i = \phi_i - \tilde{\phi}_i \quad (2.25)$$

(c) Correction coefficient as

$$\alpha_i = \sum_{j=1}^N W_{ij}^2 \quad (2.26)$$

Step 2: Repeat steps (a) to (c) for all rays.

Step 3: Identify all the rays passing through a pixel  $j$  and the corresponding values of  $W_{ij}$ ,  $\Delta\phi_i$  and  $\alpha_i$ . Let the total number of rays passing through  $j^{th}$  pixel is denoted by  $N_j$ .

Step 4: Modify the value of  $j^{th}$  pixel, for all  $j=1,2,\dots,N$ , as

$$\tilde{f}_j^k = \tilde{f}_j^{k-1} + \frac{1}{N_j} \sum_{i=1}^{N_j} \frac{\lambda W_{ij} \Delta\phi_i}{\alpha_i} \quad (2.27)$$

where  $\lambda$  denotes the relaxation factor. This complete  $k^{th}$  iteration.

Step 5: Repeat steps 1 to 4 until

$$\frac{\tilde{f}^{k+1} - \tilde{f}^k}{\tilde{f}^k} \times 100 \leq e \quad (2.28)$$

where  $e$  is the stopping criteria.



### 2.3.1.4 Anderson ART

This *algorithm*<sup>[12]</sup> is also called as simultaneous algebraic reconstruction technique (SART). SART combines both ART and SIRT.

For each view angle  $\theta$

Step 1: For each ray  $i_\theta$ , calculate

(a) The approximate projection ( $\tilde{\phi}_{i_\theta}$ ) as

$$\tilde{\phi}_{i_\theta} = \sum_{j=1}^N W_{i_\theta j} \tilde{f}_j \quad (2.29)$$

(b) Correction as

$$\Delta\phi_{i_\theta} = \phi_{i_\theta} - \tilde{\phi}_{i_\theta} \quad (2.30)$$

(c) Correction coefficient as

$$\alpha_{i_\theta} = \sum_{j=1}^N W_{i_\theta j}^2 \quad (2.31)$$

Step 2: Repeat steps (a) to (c) for all rays of view angle  $\theta$ .

Step 3: For each ray  $i_\theta$ , modify the value of  $j^{th}$  pixel, for all  $j=1,2,\dots,N$ , as

$$\tilde{f}_j^k = \tilde{f}_j^{k-1} + \frac{\lambda W_{i_\theta j} \Delta\phi_{i_\theta}}{\alpha_{i_\theta}} \quad (2.32)$$

where  $\lambda$  denotes the relaxation factor.

Step 4: Repeat step 3 for all rays of view angle  $\theta$ .

Step 5: Repeat steps 1 to 4 for all view angles. This complete  $k^{th}$  iteration.

Step 6: Repeat steps 1 to 5 until

$$\frac{f^{\tilde{k}+1} - \tilde{f}^k}{\tilde{f}^k} \times 100 \leq e \quad (2.33)$$

where  $e$  is the stopping criteria.

### 2.3.2 MART

In ART, new field value is calculated by adding correction term to the initial value. While in multiplicative ART (MART), at each iteration, a new estimate of field value is calculated by multiplication of previous value by a correction term, i.e.,

$$f_j^{k+1} = C \times f_j^k, j = 1, 2, \dots, N. \quad (2.34)$$

where  $C$  is correction term,  $f_j$  is the value of the  $j^{\text{th}}$  pixel and  $k$  is the iteration number. Depending upon the correction term, MART may be further classified in four classes, as discussed by *Verhoeven*<sup>[13]</sup>. Algorithm remains the same for all but correction term varies. Algorithm of MART may be stated as

For each iteration  $k$

Step 1: For each ray  $i$  calculate

(a) The approximate projection ( $\tilde{\phi}_i$ ) as

$$\tilde{\phi}_i = \sum_{j=1}^N W_{ij} \tilde{f}_j \quad (2.35)$$

(b) Modify the value of  $j^{\text{th}}$  pixel, for all  $j=1,2,\dots,N$ , as

$$f_j^k = C \times f_j^{k-1} \quad (2.36)$$

Step 2: Repeat steps (a) and (b) for all rays.

This complete  $k^{\text{th}}$  iteration.

Step 3: Repeat steps 1 and 2 until

$$\frac{f^{k+1} - f^k}{f^k} \times 100 \leq e \quad (2.37)$$

where  $e$  is the stopping criteria.

Four classes of MART are

- **GBH MART:** This was proposed by Gordon et al.<sup>[5]</sup>. Correction term is given by

$$C = \begin{cases} 1 - \frac{\lambda}{W_{max}}(1 - \frac{\phi_i}{\tilde{\phi}_i}) & \text{if } \tilde{\phi}_i \neq 0 \text{ and } w_{ij} \neq 0 \\ 1 & \text{else} \end{cases} \quad (2.38)$$

where  $\lambda$  is relaxation factor and  $W_{max}$  is the largest value of weight in  $W$ .

- **GH MART:** This was proposed by Gordon and Herman<sup>[14]</sup>. Correction term is given by

$$C = \begin{cases} 1 - \frac{\lambda W_{ij}}{W_{max}}(1 - \frac{\phi_i}{\tilde{\phi}_i}) & \text{if } \tilde{\phi}_i \neq 0 \text{ and } w_{ij} \neq 0 \\ 1 & \text{else} \end{cases} \quad (2.39)$$

where  $\lambda$  is relaxation factor and  $W_{max}$  is the largest value of weight in  $W$ .

- **Lent MART:** This was proposed by Lent<sup>[15]</sup>. Correction term is given by

$$C = \begin{cases} (\frac{\phi_i}{\tilde{\phi}_i})^{\lambda W_{ij}} & \text{if } \tilde{\phi}_i \neq 0 \\ 1 & \text{else} \end{cases} \quad (2.40)$$

- **Lent2 MART:** A slight modification in Lent MART leads to Lent2 MART<sup>[15]</sup>. Correction term is given by

$$C = \begin{cases} (\frac{\phi_i}{\tilde{\phi}_i})^{\lambda W_{ij}^*} & \text{if } \tilde{\phi}_i \neq 0 \\ 1 & \text{else} \end{cases} \quad (2.41)$$

where  $W_{ij}^*$  is given by  $\frac{W_{ij}}{W_{max}}$ .

## 2.4 Convergence criteria

It is necessary to determine when an iterative algorithm has converged to a solution which is optimal. In all algorithm, iterations are carried out until the following relation is satisfied

$$\frac{f^{k+1} - f^k}{f^k} \times 100 \leq e \quad (2.42)$$

where,  $e$  is equal to 0.01. Here  $f^{k+1}$  is the field value at  $(k+1)^{th}$  iteration and  $f^{th}$  is the field value at  $k^{th}$  iteration.

## 2.5 Error indicators

Four error measures were used. They are used to find the deviation of reconstructed field from the exact field. Different algorithms may be compared on the basis of error measures. Lesser is the error induced by an algorithm in reconstructing a field, better is that algorithm. These can be applied only to the simulated field since we know the exact field. CosGauss phantom is used for the error analysis of ART and MART. If  $f_j$  is the exact value of  $j^{th}$  pixel and  $\tilde{f}_j$  is the reconstructed value of  $j^{th}$  pixel, then the errors may be defined as

1. AVERAGE ERROR:

$$a = \frac{\sum_{j=1}^N |f_j - \tilde{f}_j|}{N} \quad (2.43)$$

2. NORMALIZED RMS ERROR:

$$d = \left\{ \frac{\sum_{j=1}^N [f_j - \tilde{f}_j]^2}{\sum_{j=1}^N [f_j - \bar{f}]^2} \right\}^{1/2} \quad (2.44)$$

where  $\bar{f}$  is the average value of geometry used. The RMS error is large if there are few large errors in reconstruction.

3. NORMALIZED ABSOLUTE ERROR:

$$r = \frac{\sum_{j=1}^N |f_j - \tilde{f}_j|}{\sum_{j=1}^N |f_j|} \quad (2.45)$$

This shows the effect of many small errors.

4. MAXIMUM ERROR:

It is the largest difference between original and reconstructed field value.

It may be defined as

$$E = \max |f_j - \tilde{f}_j| \quad \text{for } j=1,2,\dots,N \quad (2.46)$$

# Chapter 3

## Experimental setup

The experimental unit consists of a collimator and a detector. Both are housed in the lead ring, whose inner diameter is 152 mm and outer diameter is 252 mm. This unit can be used for collecting data for parallel beam geometry. The platform, on which specimen is placed, can have vertical movement of 105 mm and horizontal movement of 75 mm. It can also be rotated with a least count of  $2^\circ$ . Thus, this unit can have two translational and one rotational motions. The other equipments used are NaI scintillation detector, high voltage unit, low voltage unit, linear amplifier, single channel analyzer, timer, scalar. The source used is  $Cs^{137}$ . Experimental set up is shown in block diagram 3.1.

### 3.1 Equipment

The detail description of the equipment used in the experiment is given in the following sub-sections :

#### 3.1.1 Scintillation detector

There are certain materials, e.g. organic, inorganic and plastic, which emit flashes of light or scintillations when radiation passes through them. These scintillations can be used to detect any type of radiations but are mostly used

for  $\gamma$ -ray counting. The output of a scintillator is proportional to the incident energy and hence can be used to find the energy of a  $\gamma$ -ray.

*Radiation is absorbed in the scintillator when it strikes the material.* The absorbed energy is utilized in lifting the electrons to the excited state and part of it appears as heat energy. The electrons in the excited state de-excite in a very short time of about  $10^{-8}$ , leading to emission of light. This de-excitation time varies from material to material.

The intensity of the emitted light is directly proportional to the energy lost by the incident radiation. The emitted light flashes are amplified by a photo multiplier. The photo multiplier tube consists of a photo cathode and several dynodes, each of which is maintained at a successively higher voltage. The photo cathode is usually a thin coating of Antimony-Cesium on the inside surface of the photo multiplier, whereas the dynodes are Antimony-Cesium, Silver-Magnesium or Copper-Beryllium. The electrons emitted by the photo cathode are amplified by releasing more electrons at each of the dynodes. The electrons from the last dynode are focused on to the anode connected to the preamplifier. The coupling of the scintillator to the photo multiplier is done by a light pipe. Normally, the scintillator is covered with a highly reflecting material, such as MgO and  $Al_2O_3$ , to avoid loss of light pulses. The light pipe is commonly made of glass, lucite or plexiglass. Its main purpose is to transmit efficiently the light pulses to photo cathode of photo multiplier tube.

The advantages of scintillator for detecting  $\gamma$ -ray are:

- Since all the light pulses are emitted in a very short time, the scintillator integrates these into a single pulse. The height of this pulse is proportional to the incident  $\gamma$ -ray energy.
- Since the scintillator is solid, it has more atoms per unit volume than a gas-filled detector, leading to a better detection.
- Since the time constant of the scintillator is small, its dead-time is very small, facilitating a high rate.
- A large scintillator increases the probability of absorbing the scattered  $\gamma$ -rays, leading to an increase in photo peak efficiency.

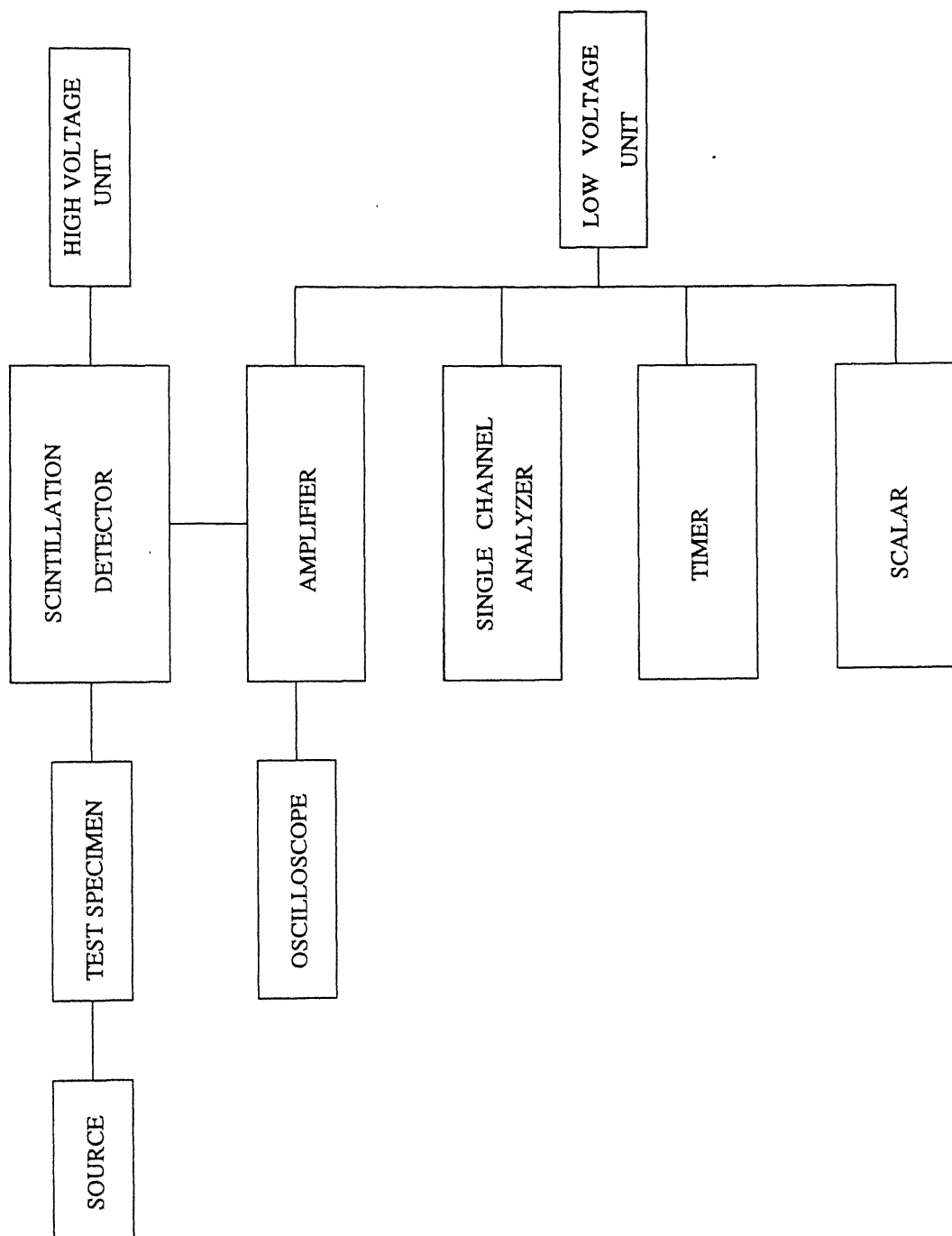


Figure 3.1: Experimental set-up

A disadvantage in using a scintillator is the decrease in the light output with an increase in the energy of the incident  $\gamma$ -radiation. For example, the NaI (Tl) scintillator displays 20% variation in the light output per unit energy of  $\gamma$ -ray over the range of 0-1 MeV. The light output also varies greatly with the type of radiation. With the NaI (Tl) scintillator, the electrons give a better response than alpha-particles of same energy.

The overall efficiency of a scintillator is low because the detection process, namely, radiation causes light emission which is then reconverted into electrons at the photo cathode, is complex. Typically 300 eV of energy is dissipated in the NaI (Tl) scintillator for release of one photo electron, whereas in an organic scintillator about 1-5 KeV energy per electron is required. The corresponding energy for producing an ion-pair in a gas-filled detector is 30 eV and in a semiconductor is 4 eV. Scintillators are of many types, e.g. disk-type, right circular cylinder and well-type.

### 3.1.2 Linear amplifier

It amplifies the output pulses from the detector. It has three gain controls, namely

- **Input attenuator**, which have attenuation factors of 1,2,5,10,20 and 50.
- **Coarse gain**, which have amplification factors of 0.1, 0.3, 1.
- **Fine gain**, with an amplification factors of 1-3.
- **Time constants**, the pulse shaping provision of linear amplifier has variable integrating time constants of 0.1, 0.2, 0.5, 1, 2, 5  $\mu$ sec.

### 3.1.3 Voltage units

- **High voltage unit**: It supplies high voltage from the range of 300 to 2500v.



- **Low voltage unit** : It supplies low voltage, ranging from -24 to +24.

### 3.1.4 Single channel analyzer (SCA)

An SCA can operate either in *integrating (INT)* or *differentiating (DIFF)* mode. In the INT mode, the lower level (base line) of the SCA acts as the discriminating bias. In the DIFF mode, the lower level is set at  $E$  and upper level at  $E + \Delta E$ , so that only the signal with a pulse height between  $E$  and  $E + \Delta E$  is counted by the scalar. The window  $\Delta E$  can be continuously varied from 0 to 2 V. The base line adjustable between 0.2 to 10 V, thus making it possible to resolve and identify any pulse amplitude in this range. The output of SCA is constant and is of magnitude 10 V.

### 3.1.5 Timer

It sets the duration for which the counting is to be done. The factors are 1, 2, 5 multiplied by 10 sec, 100 sec and 1000 sec.

### 3.1.6 Scalar

It is used to count the signals of pulse height between  $E$  and  $E + \Delta E$ .

## 3.2 Data collection

Data collection using  $\gamma$ -ray CT scanner is done through following steps:

- **Identification of photo peak of the source**

Connect the low voltage and high voltage unit to the preamplifier of the scintillation head. Connect preamplifier to the linear amplifier. Connect the output from amplifier to single channel analyzer (SCA). Output from SCA is given to scalar through timer. Turn on the high voltage unit

and slowly increase its voltage to 750 V. Place the source through a collimator. Set window ' $\Delta E$ ' to 0.5 V and slowly increase the base from 0.1 V. Set timer at 10 sec and collect the data at each base line setting. The counts will be higher at the photo peak of the source.

- **Collection of data**

Set the window and the base line at which photo peak was identified. Place the object between the source and detector on the platform. Set the timer at 100 sec and collect the data using parallel beam geometry collection mode.

### *Setting of apparatus*

- *Polarity*= -ve
- *Attenuator*=20
- *Gain*=1
- *Time constant*=5  $\mu$ sec
- *Window width*=0.5 V
- *Base line*=4.0 V
- *Mode*= Differentiating
- *Timer*= 100 sec
- *High voltage unit*= 750 V

## 3.3 Sources of error

1. The detector must sense only those photons coming straight from the source. However, due to scattering some additional photons enter the detector, thereby increasing the count rate. Thus, density predicted by experimental results will be different from the true density of material. Radiation from these deflected photons is called secondary radiation.

2. Sources must be of small size in order to reduce scattering and geometric unsharpness.
3. voltage fluctuation leads to shift in photo peak, or in other words there is fluctuation of  $N_0$  within a single pass.
4. Lateral displacement of object by 1 mm, may not displace it exactly by 1 mm due to gear mechanism. This may be true with rotational motion also.

### 3.4 Precautions

1. Counts must be taken for higher time period, to reduce error.
2. To minimize error due to voltage fluctuation, each pass should be preceded and succeeded by taking the value of  $N_0$ . If there is large variation in counts, the experiment for that case must be repeated else the average of the two values must be taken as the final value of  $N_0$ .
3. To avoid backlash, object should be lateraly displaced and rotated in only one direction.
4. The object should not be distrubed from its position till data collection completes.
5. Source strength should be adequate for large  $N_0$ .

# Chapter 4

## Validation of Programs

### 4.1 Simulated data

The programs for ART and MART have been tested on simulated data. **CosGauss phantom** is used to compare different forms of ART and MART. CosGauss phantom is generated using the equation

$$\begin{aligned} \text{CosGauss}(x, y) = & \zeta [0.3 \cos(x, y) + 0.8 (\exp\{-[9(x - x_1)]^2 - [6(y - y_1)]^2\} \\ & + \exp\{-[8(x - x_2)]^2 - [(y - y_2)]^2\})] \end{aligned} \quad (4.1)$$

where,

$$\begin{aligned} \cos(x, y) = & 0.25 \{1 - \cos[2\pi(x + 0.5)^{4/5}]\} \\ & \times \{1 - \cos[2\pi(y + 0.5)^{2/3}]\} \quad \text{for } |x|, |y| < 0.5 \\ = & 0 \quad \text{else} \end{aligned} \quad (4.2)$$

Thus, CosGauss phantom is the weighted superposition of the cosine phantom and two Gaussian peaks centered at  $x_1=0.20$ ,  $y_1=0.10$ ,  $x_2=-0.20$  and  $y_2=-0.35$ . Here,  $\zeta$  is normalizing factor and is equal to 1.09. CosGauss phantom is shown in surface and contour plots in Figs. 4.1. The contour plot has the same contour levels. **The contour interval is 0.1 units.**

A number of limited and unlimited data **imaging geometries** are used which are shown in Table 4.1. These may be basically divided into four categories:

1. **Limited angle with a limited number of views**, in which both the

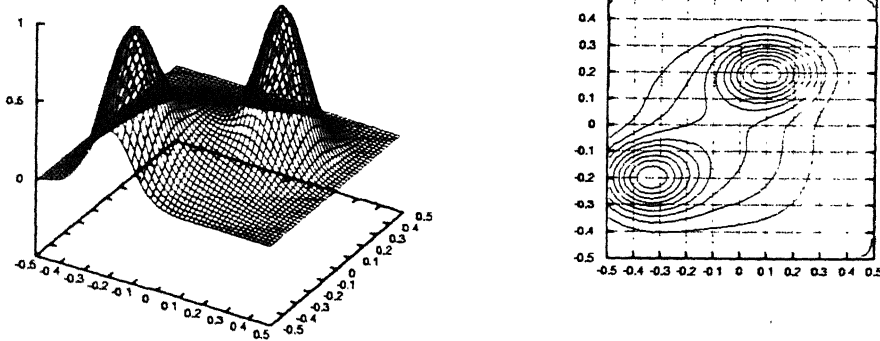


Figure 4.1: CosGauss phantom

- number of views and the possible viewing angle are restricted, e.g. cases A, B, C.
2. **Limited angle with unlimited number of views**, where viewing angle is restricted but number of views are not, e.g. case D.
  3. **Unlimited angle with a limited numbers of views**, in which number of views are restricted but the total viewing angle is not, e.g. cases E, F.
  4. **Unlimited angle with unlimited number of views**, where both the number of views and possible viewing angle are not restricted, as in case I.

The field to be reconstructed is discretized into  $50 \times 50$  square grids of equal size. **ART** and **MART** performances are compared using case F, where, data sets consist of projections at five angles equally spaced over the viewing angle of  $180^\circ$  ( $0^\circ, 36^\circ, 72^\circ, 108^\circ, 144^\circ$ ). In all 312 rays are considered for 5 projections. The ray location is chosen such that the ray spacing, perpendicular distance between rays, remains same for all views. Ray spacing equals to the dimension of a pixel.

Cases	Projections	No. of rays	View angle
A	2	100	90
B	3	170	90
C	5	294	90
D	10	616	90
E	4	240	180
F	5	312	180
G	9	566	180
H	10	624	180
I	18	1132	180

Table 4.1: Imaging geometries

Table 4.2 compares the performance of **ART** family for relaxation factor 0.5 while Table 4.3 compares the members of **MART** family at relaxation factor 1.0. **GBH** does not converge for higher values of relaxation factor. *Oscillating pattern* of GBH during iterative process is shown in Fig. 4.2 for relaxation parameter 0.01. Table 4.4 shows the performance of GBH at relaxation parameter 0.001 for convergence criteria 0.05 and at relaxation parameter 0.0001 for convergence criteria 0.01.

5 Projections, 312 rays, 180 view angle, $\lambda = 0.5$						
Algorithms of ART	Average error (%)	Normalized RMS error (%)	Normalized absolute error (%)	Maximum error	CPU time ( s )	Iterations
Mayinger	10.54	59.12	55.57	0.4280	8.13	6
Gordan	10.11	55.31	53.31	0.4084	9.74	8
Gilbert	6.90	38.34	36.40	0.4113	40.53	39
Anderson	10.11	55.32	53.29	0.4090	9.31	7

Table 4.2: Performance of ART for CosGauss phantom

The reconstructed images of CosGauss phantom by these eight algorithms are shown in Figs.4.3 to 4.10.

Effect of *relaxation parameter on errors* is shown in Tables 4.5 and 4.6 for **Gilbert ART** and **Lent2**, respectively. Here, relaxation parameter is varied from 0.01 to 1.99 and the corresponding variations in errors are studied.

5 Projections, 312 rays, 180 view angle, $\lambda = 1$						
Algorithms of MART	Average error (%)	Normalized RMS error (%)	Normalized absolute error (%)	Maximum error	CPU time ( s )	Iterations
GBH	-	-	-	-	-	-
GH	1.55	11.00	8.18	0.1869	1294	1791
Lent	1.27	8.43	6.69	0.1083	324.64	432
Lent2	1.05	7.51	5.53	0.1082	114.37	149

Table 4.3: performance of MART for CosGauss phantom

5 Projections, 312 rays, 180 view angle, $\lambda = 0.001$ , convergence=0.05						
Algorithm	Average error (%)	Normalized RMS error (%)	Normalized absolute error (%)	Maximum error	CPU time ( s )	Iterations
GBH	3.73	25.69	19.65	0.3623	241.36	335

5 Projections, 312 rays, 180 view angle, $\lambda = 0.0001$ , convergence=0.01						
Algorithm	Average error (%)	Normalized RMS error (%)	Normalized absolute error (%)	Maximum error	CPU time ( s )	Iterations
GBH	3.55	24.37	18.73	0.3214	1293.6	1780

Table 4.4: performance of GBH for CossGauss phantom

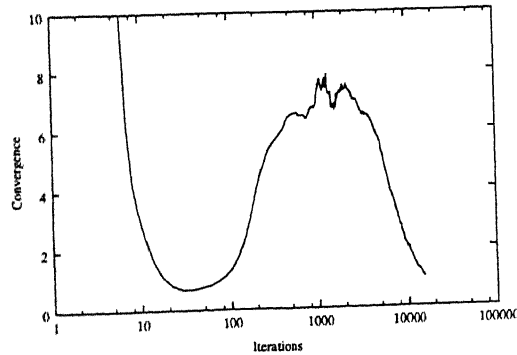


Figure 4.2: Oscillating pattern of GBH

CosGauss phantom is reconstructed using **Gilbert ART** and **Lent2** for

Gilbert ART for 5 projections, view angle 180					
$\lambda$	Iterations	Average error (%)	Normalized RMS error (%)	Normalized absolute error (%)	Maximum error
0.01	548	7.35	46.12	38.77	0.5676
0.1	119	6.62	38.28	34.90	0.4583
0.5	39	6.90	38.34	36.40	0.4113
1.0	24	8.10	43.22	42.73	0.4060
1.5	18	12.88	66.04	67.93	0.5042
1.99	3	17.86	87.69	94.20	0.5813

Table 4.5: Variation of errors with relaxation parameter for Gilbert ART

all the imaging geometries mentioned in Table 4.1. Tables 4.7 and 4.9 show the *variation of CPU time and iterations with the number of projections* for **Gilbert ART** and **Lent2**, respectively. Dependence of different errors, in the reconstructed field, on the number of projections is mentioned in Tables 4.8 and 4.10 for these two algorithms.

Reconstruction of CosGauss phantom, with projection sets of cases C and I, are shown in Figs. 4.11 and 4.12 for Gilbert ART and in Figs. 4.13 and 4.14 for Lent2.

lent2 for 5 projections, view angle 180					
$\lambda$	Iterations	Average error (%)	Normalized RMS error (%)	Normalized absolute error (%)	Maximum error
0.01	730	1.29	8.52	6.78	0.1062
0.1	179	1.224	8.14	6.46	0.1105
0.5	250	1.06	7.32	5.60	0.1104
1.0	149	1.05	7.51	5.53	0.1082
1.5	213	1.13	8.54	5.97	0.1253
1.99	657	1.06	7.56	5.60	0.1104

Table 4.6: Variation of errors with relaxation parameter for Lent2

**Lent2** is further applied to reconstruct physical objects with internal features. The field to be reconstructed is discretized in  $50 \times 50$  pixels and



Gilbert ART for $\lambda = 0.5$		
Case	CPU time(s)	Iterations
A	6.53	21
B	16.91	32
C	32.64	34
D	71.11	35
E	27.66	36
F	40.53	39
G	76.06	40
H	84.41	40
I	155.89	42

Table 4.7: Variation of iterations and CPU time of Gilbert ART

projection sets of cases C, F, I, are used for reconstruction. The different simulated objects used are:

1. **Circular plate with a central hole.** This simulation is an object with absorption coefficient 1 everywhere outside the hole and 0 inside the hole. Circular plate is of diameter 50 units and holes have diameter of 20 units. Surface and contour plots of this simulated object are shown in Fig. 4.15. Reconstructed images are shown in Fig. 4.16.

Gilbert ART for $\lambda = 0.5$				
Case	Average error (%)	Normalized RMS error (%)	Normalized absolute error (%)	Maximum error
A	11.76	69.79	62.01	0.5267
B	7.42	45.21	39.13	0.4829
C	7.38	42.96	38.94	0.4334
D	7.35	42.56	38.76	0.4334
E	6.69	36.76	35.26	0.3961
F	6.90	38.34	36.40	0.4113
G	6.37	34.10	33.62	0.3749
H	6.37	34.08	33.58	0.3363
I	6.09	31.92	32.11	0.2622

Table 4.8: Errors in Gilbert ART

Lent2 for $\lambda = 1.0$		
Cases	CPU time(s)	Iterations
A	3.96	14
B	5.81	12
C	139.55	193
D	537.73	366
E	9.34	14
F	114.37	149
G	238.81	172
H	355.04	233
I	1407.17	522

Table 4.9: Variation of Iterations and CPU time with projections in Lent2

2. **Square plate with five holes**, this is simulated by considering absorption coefficient 1 outside the holes and 0 inside the holes. Size of plate is  $50 \times 50$  units and holes have diameter of 10 units. This is shown in surface and contour plots in Fig. 4.17. The reconstructed images are shown in Fig. 4.18. The plot of 11<sup>th</sup>, 26<sup>th</sup> and 41<sup>st</sup> rows of the exact and the reconstructed field for cases C, F, I are shown in Figs. 4.19 to 4.21.

Here, the field values are either 0 or 1. The case in which the field values are widely separated is also studied. In which, holes have absorption coefficient 10 and plate has absorption coefficient 100. This case simulates a highly dense object with less denser materials embedded in it. The ability of algorithm to predict the presence of defects in denser media have been studied. The plots of 11<sup>th</sup>, 26<sup>th</sup> and 41<sup>st</sup> rows of exact field and the reconstructed field for cases C, F, I are shown in Figs. 4.22 to 4.24.

3. **Square plate with two holes**, this is similar to the object 2, except that it has only two holes. Object 2 is symmetrical while this object is non-symmetrical. This case have been considered to study the reconstruction of a non-symmetrical field. Fig. 4.25 shows the surface and contour plots of this object and the reconstructed fields in the form of contours are shown in Fig. 4.26.

Lent2 for $\lambda = 1.0$				
Cases	Average error (%)	Normalized RMS error (%)	Normalized absolute error (%)	Maximum error
A	9.52	65.62	50.18	0.4632
B	2.75	17.90	14.51	0.1407
C	1.11	8.02	5.85	0.1164
D	0.94	6.89	4.98	0.0998
E	1.13	7.20	5.98	0.0738
F	1.05	7.51	5.53	0.1082
G	0.65	4.64	3.44	0.0693
H	0.57	4.17	2.98	0.0643
I	0.36	2.57	1.88	0.0418

Table 4.10: Errors in Lent2

4. **Square plate with five circular inclusions**, in the above cases, the field values are either 0 or 1 which clearly distinguishes the holes from the object. This case have been used to see whether the algorithm is able to reconstruct a field , whose values are closer to each other. Here, square plate has absorption coefficient 1 and inclusions have slightly higher absorption coefficient of 1.2. Fig. 4.27 shows the distribution of field values and the reconstructions are shown in Fig. 4.28.

## 4.2 Experimental data

The object, scanned by the  $\gamma$ -ray CT scanner, was made of plexi-glass, whose cross-sectional area was 2.5 cm $\times$ 2.5 cm and was 1.5 cm thick. It has five holes, each of diameter 4 mm. Aim of the experiment is to reconstruct one plane of this object. It may be thus assumed as a square plate of size 2.5 cm by 2.5 cm with five holes. The field to be reconstructed is divided into 25 $\times$ 25 grids. The spacing between the rays is 1 mm, since the object is displaced horizontally by 1 mm.

Object was scanned by taking projections at 12 angles equally spaced over 180°. In all 368 rays were taken. The object field ( $\mu$ ) was reconstructed

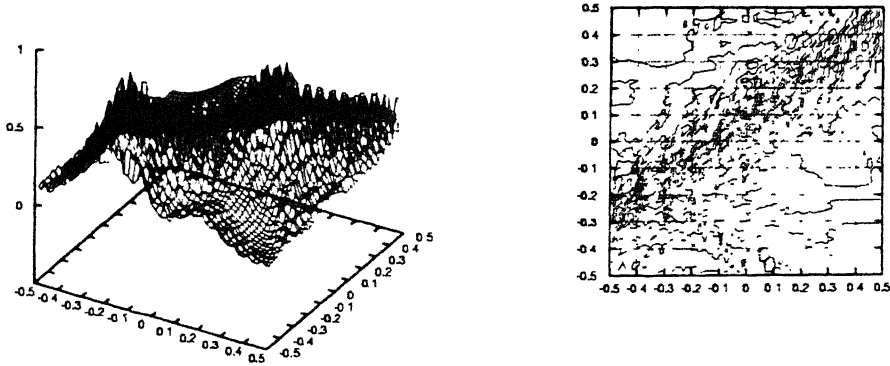


Figure 4.3: Mayinger ART reconstruction of CosGauss phantom using case F

using Lent2. The reconstructed field is the distribution of absorption coefficient.

Field is reconstructed for the following cases:

1. Projections at two angles, i.e.  $0^\circ$ ,  $90^\circ$ . Total rays are 48.
2. Projections at four angles, i.e.  $0^\circ$ ,  $45^\circ$ ,  $90^\circ$ ,  $135^\circ$ , and the total rays considered are 116.
3. Projections at 12 angles and the total rays are 368.

Reconstructed fields for the above three cases are shown in Figs. 4.29 to 4.31. All the contour plots have the same contour levels, **the contour interval is 0.013 units**. Plots for 6<sup>th</sup>, 12<sup>th</sup>, 18<sup>th</sup> rows of the reconstructed fields, by 4 views and 12 views, are shown in Figs. 4.32 to 4.37.

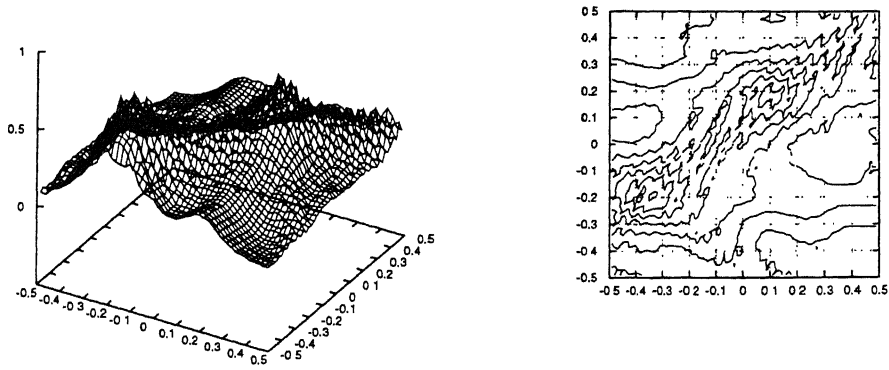


Figure 4.4: Gordon ART reconstruction of CosGauss phantom using case F

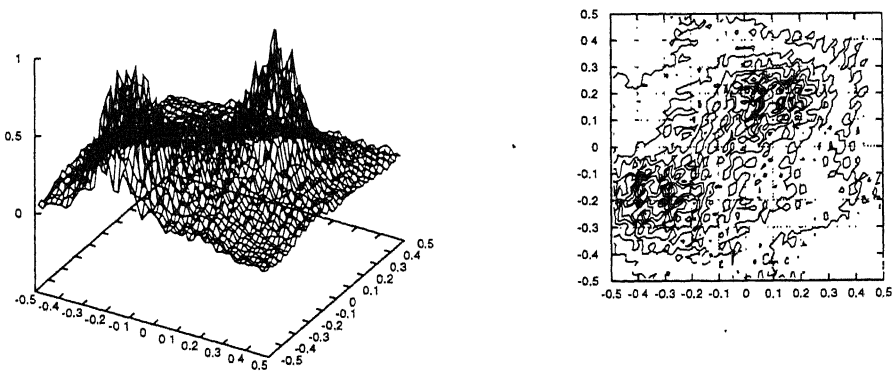


Figure 4.5: Gilbert ART reconstruction of CosGauss phantom using case F

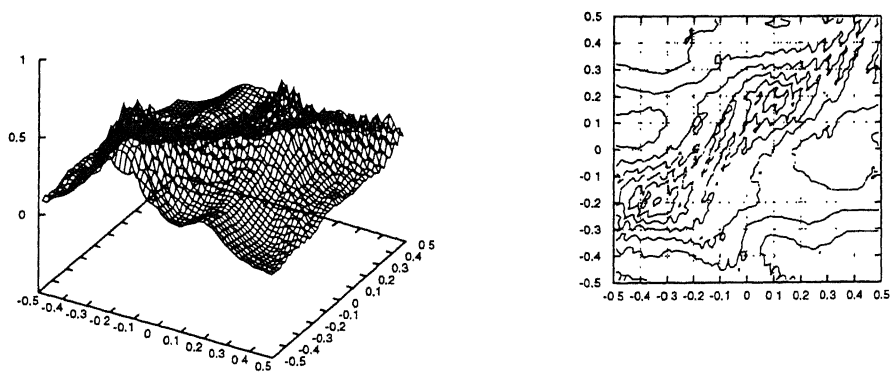


Figure 4.6: Anderson ART reconstruction of CosGauss phantom using case F

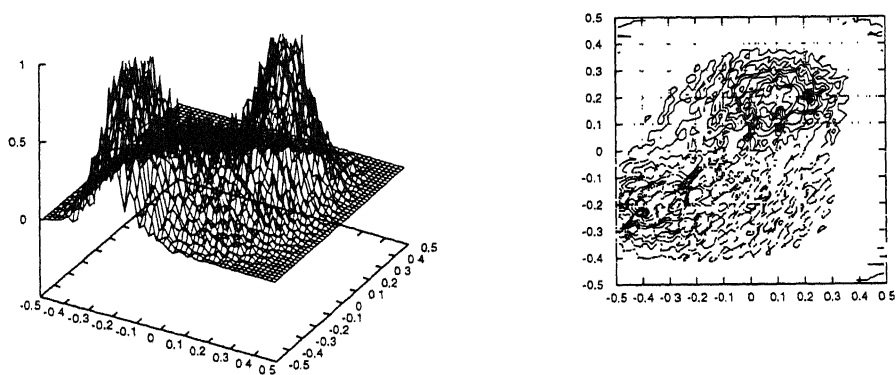


Figure 4.7: GBH reconstruction of CosGauss phantom using case F

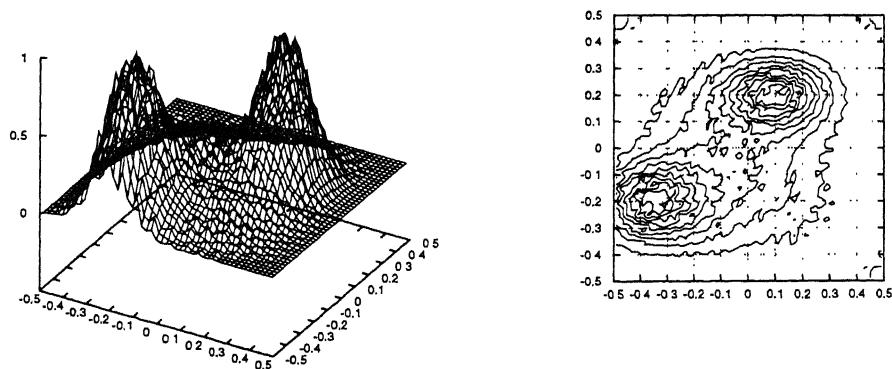


Figure 4.8: GH reconstruction of CosGauss phantom using case F

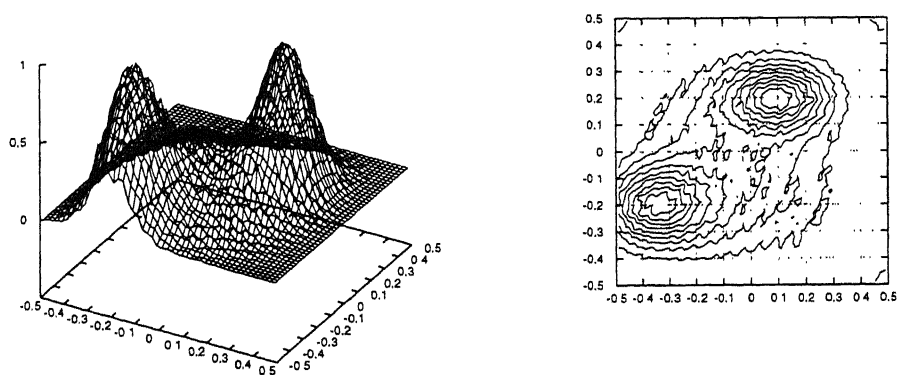


Figure 4.9: Lent reconstruction of CosGauss phantom using case F

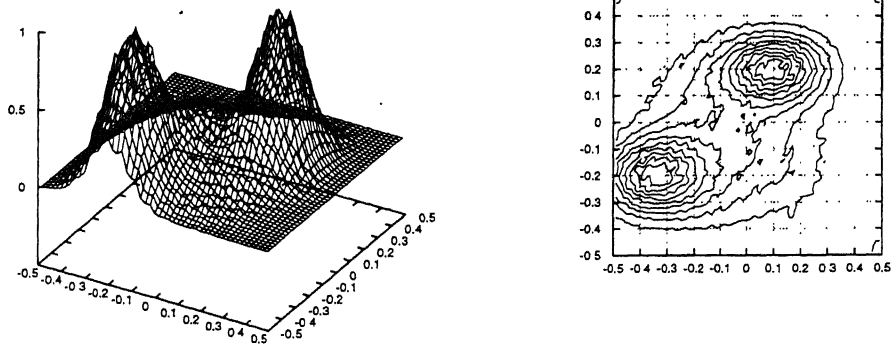


Figure 4.10: Lent2 reconstruction of CosGauss phantom using case F

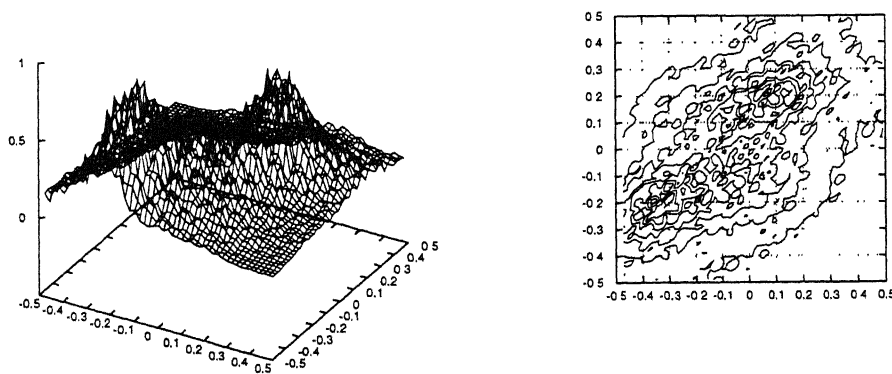


Figure 4.11: Gilbert ART reconstruction of CosGauss phantom using case C



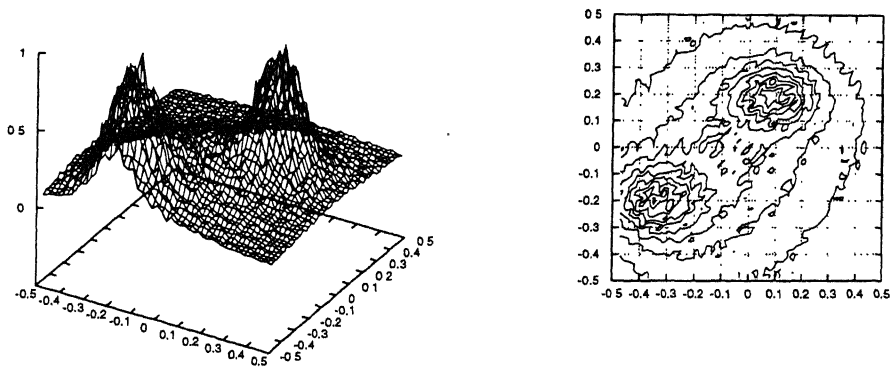


Figure 4.12: Gilbert ART reconstruction of CosGauss phantom using case I

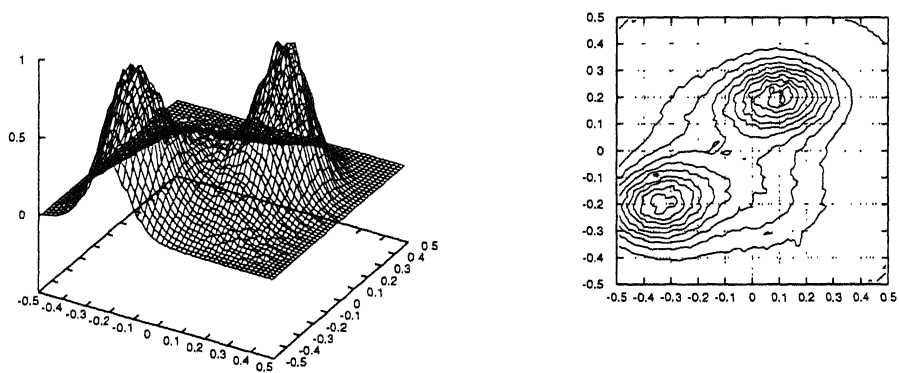


Figure 4.13: Lent2 reconstruction of CosGauss phantom using case C

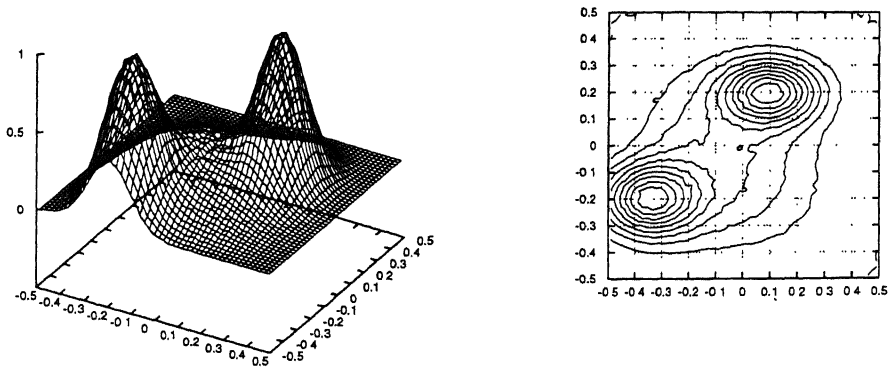


Figure 4.14: Lent2 reconstruction of CosGauss phantom using case I

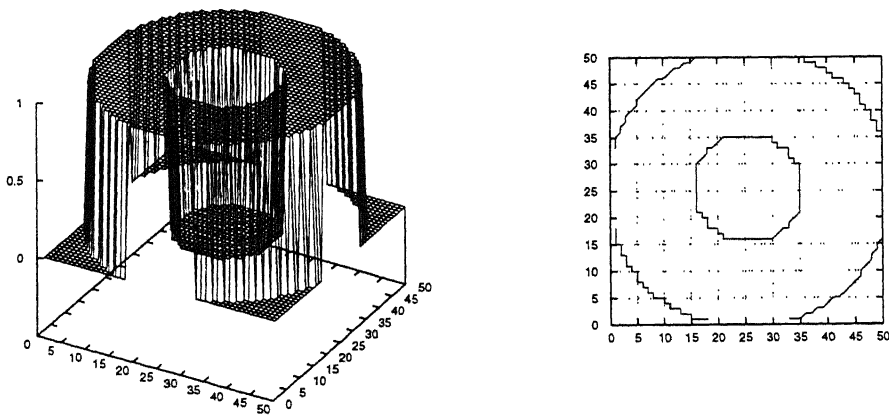
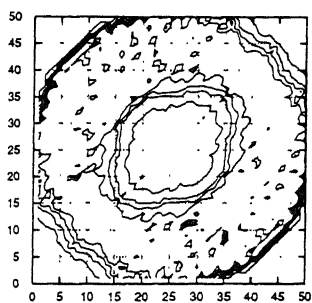
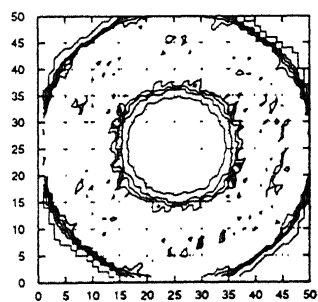


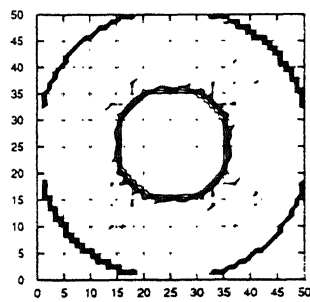
Figure 4.15: Circular plate with circular hole



(a)



(b)



(c)

Figure 4.16: Reconstruction of a circular plate with circular hole using (a) case C, (b) case F, (c) case I

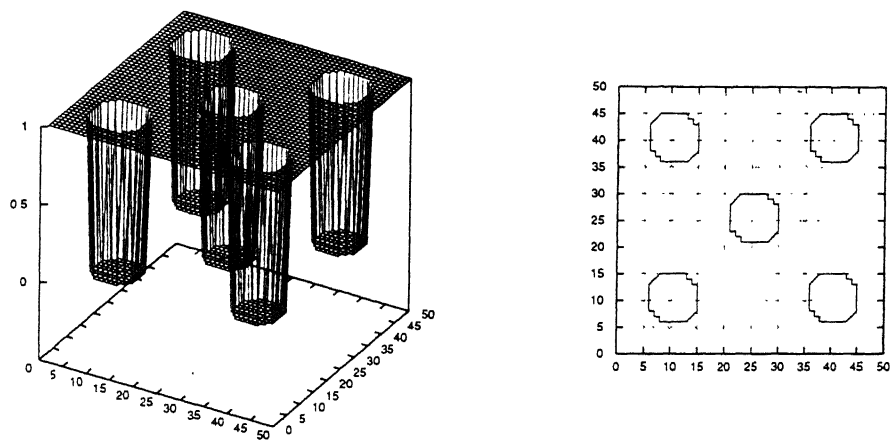


Figure 4.17: Square plate with five holes

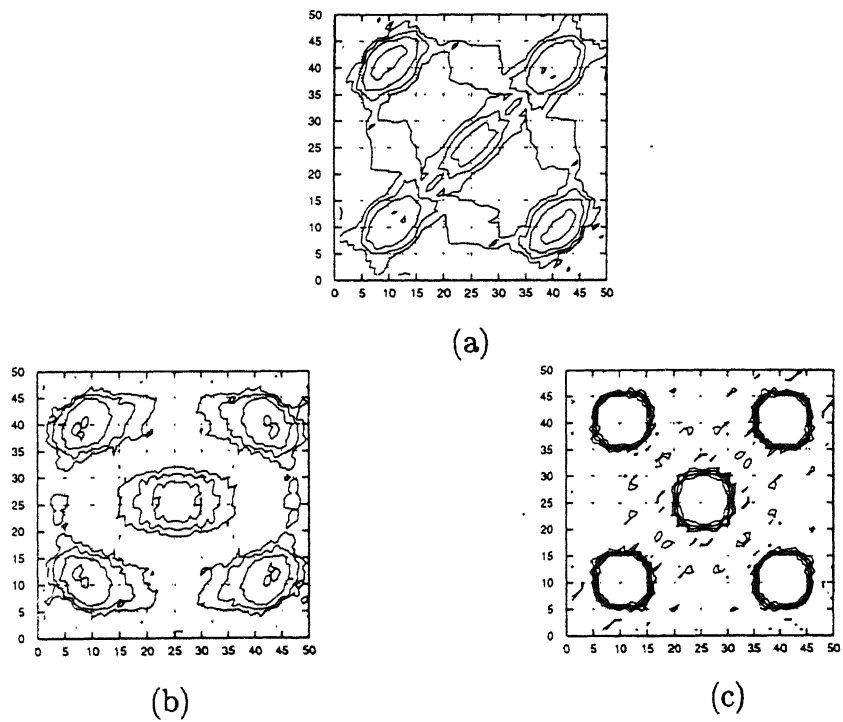
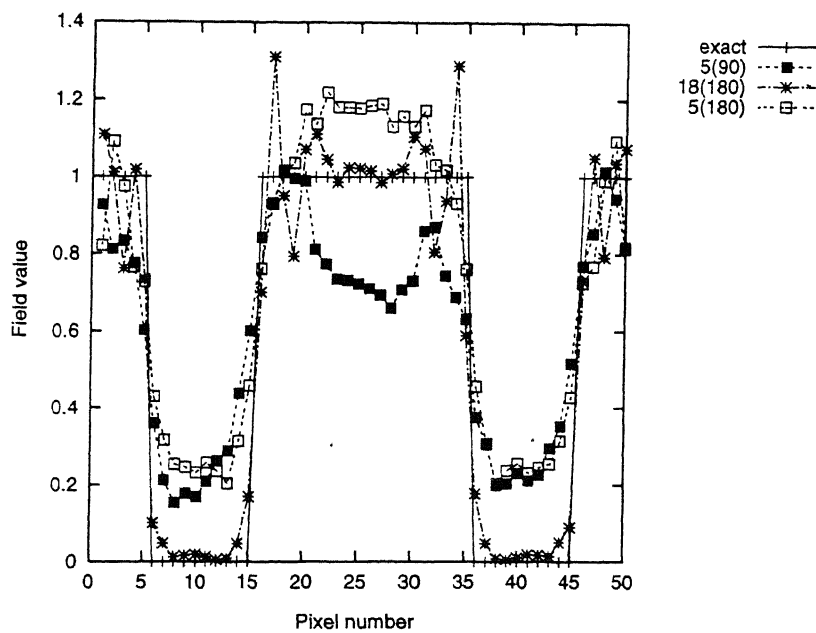
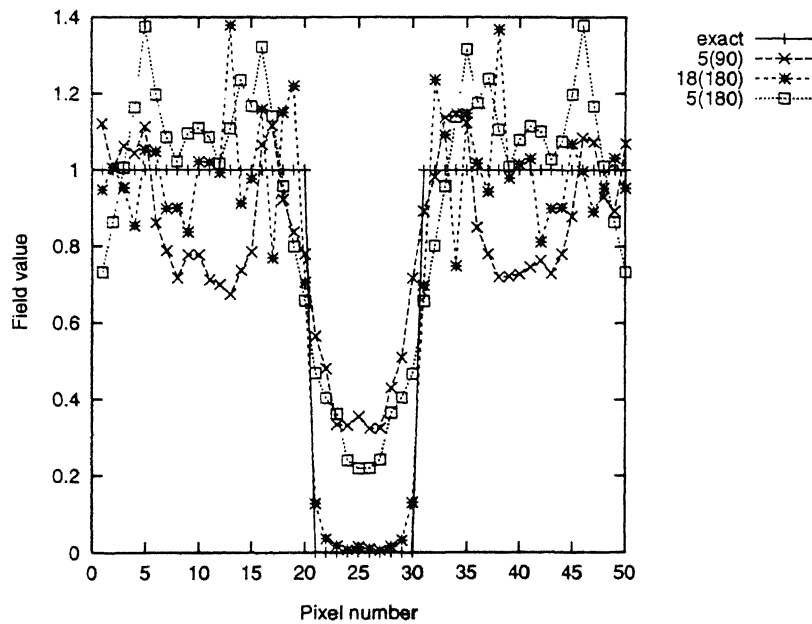
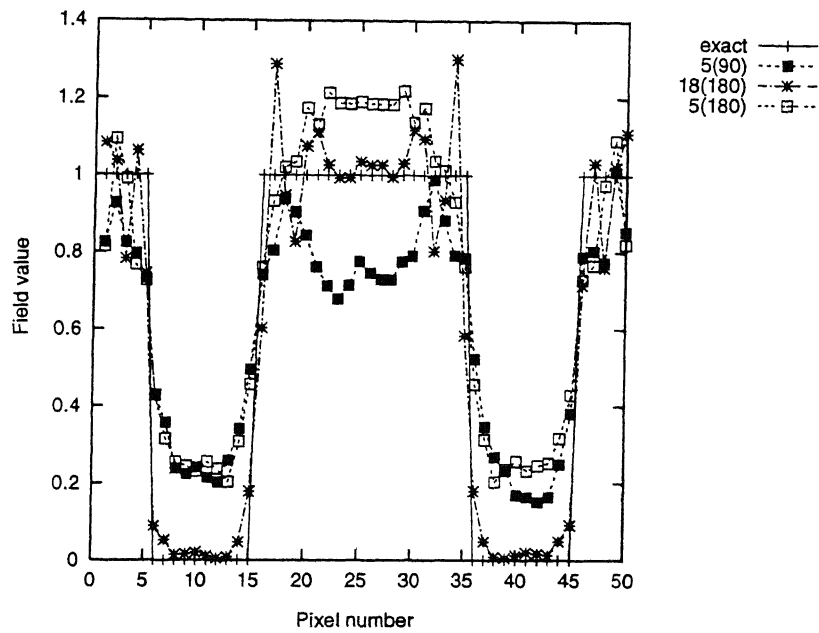
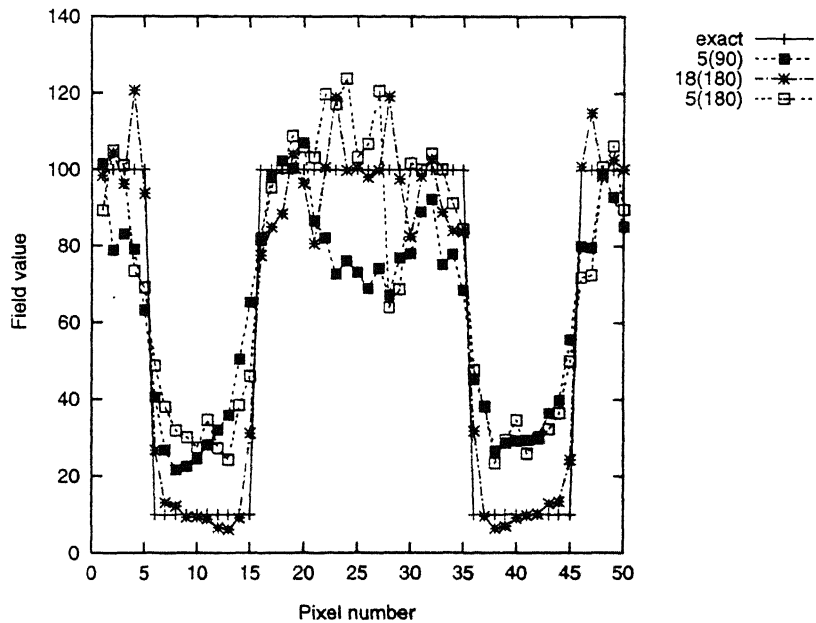
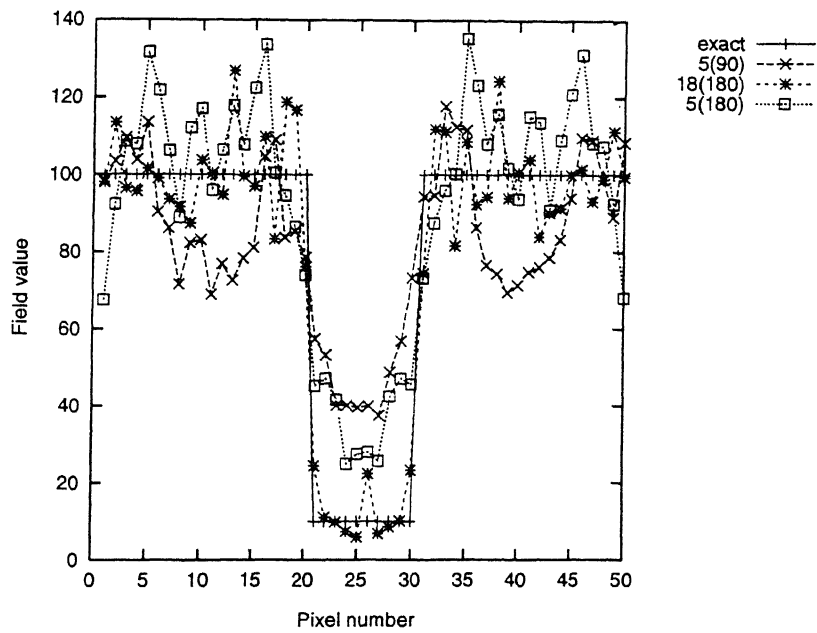
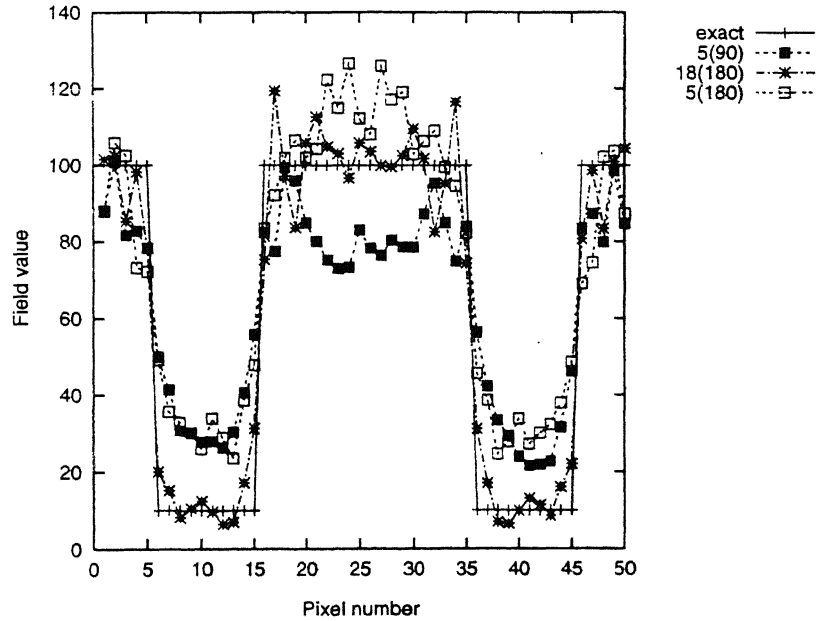


Figure 4.18: Reconstruction of square plate with five holes using (a) case C, (b) case F, (c) case I

Figure 4.19: Line plots of the 11<sup>th</sup> rowsFigure 4.20: Line plots of the 26<sup>th</sup> rows

Figure 4.21: Line plots of the 41<sup>st</sup> rowsFigure 4.22: Line plots of the 11<sup>th</sup> rows

Figure 4.23: Line plots of the 26<sup>th</sup> rowsFigure 4.24: Line plots of the 41<sup>st</sup> rows

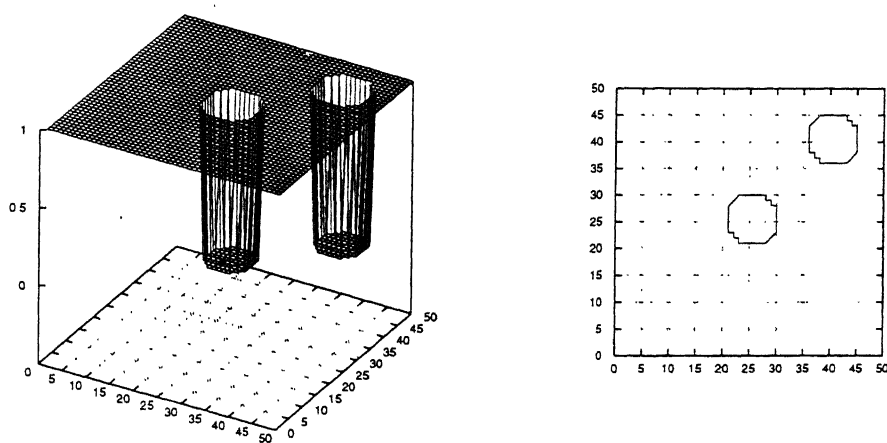


Figure 4.25: Square plate with two holes

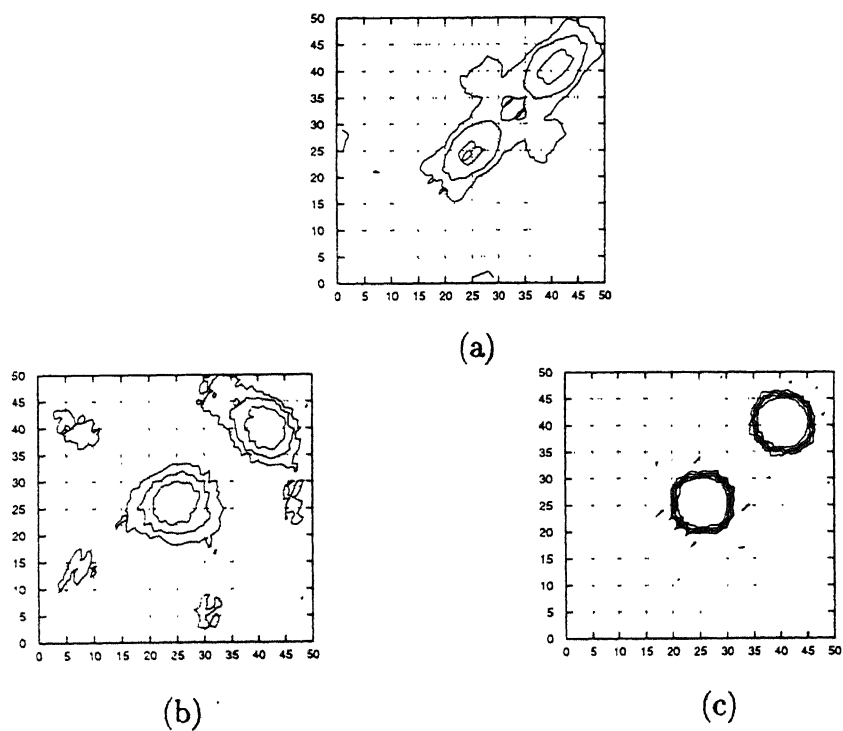


Figure 4.26: Reconstruction of square plate with two holes using (a) case C, (b) case F, (c) case I



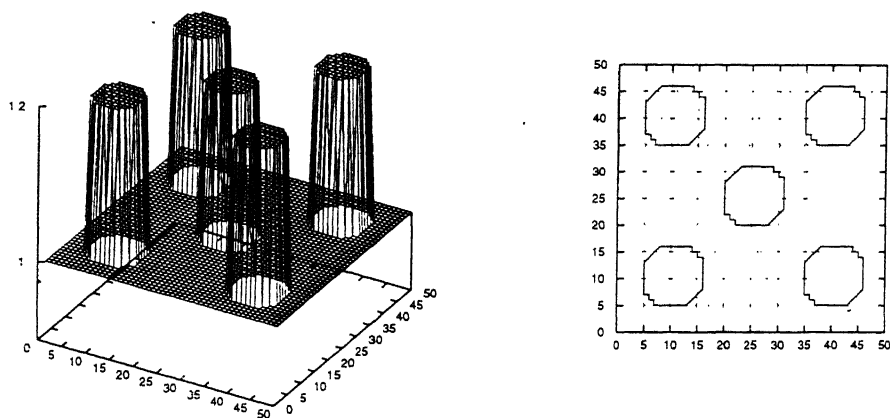


Figure 4.27: Square plate with five inclusions

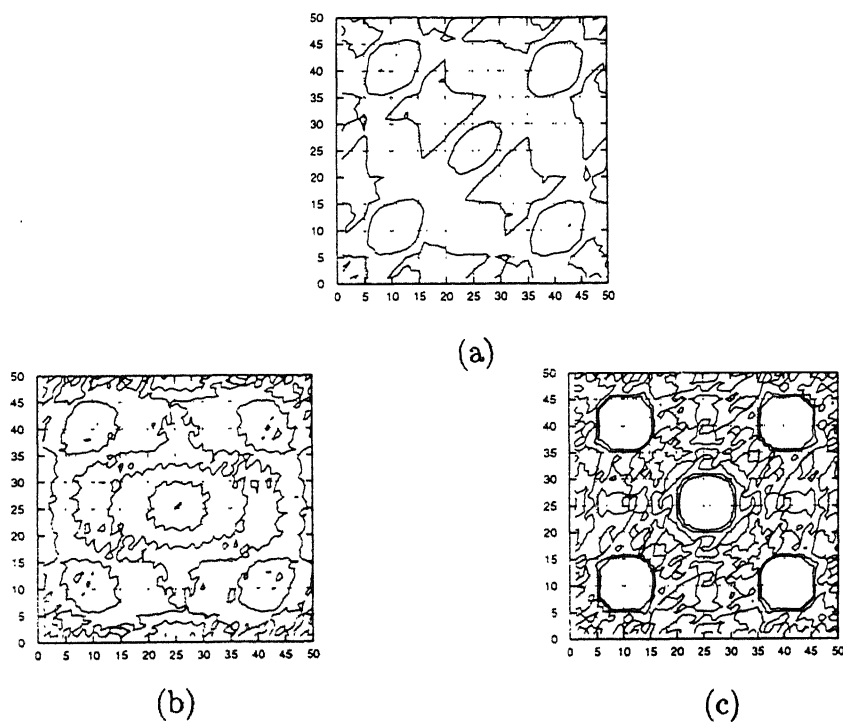


Figure 4.28: Reconstruction of square plate with five inclusions using (a) case C, (b) case F, (c) case I

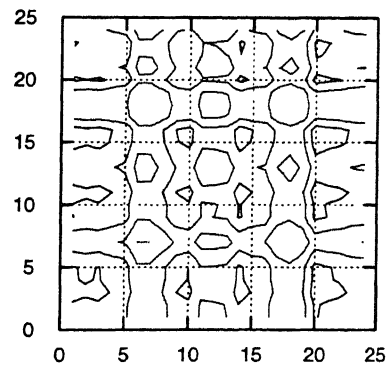


Figure 4.29: Reconstruction with 2 views

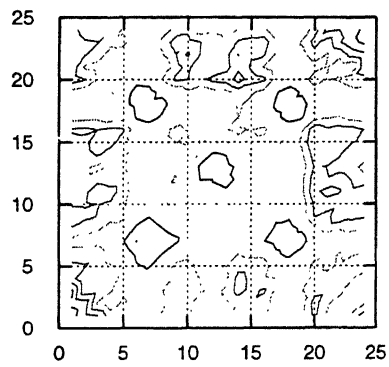


Figure 4.30: Reconstruction with 4 views

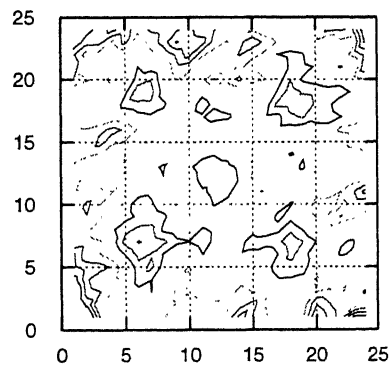


Figure 4.31: Reconstruction with 12 views

Experimental results

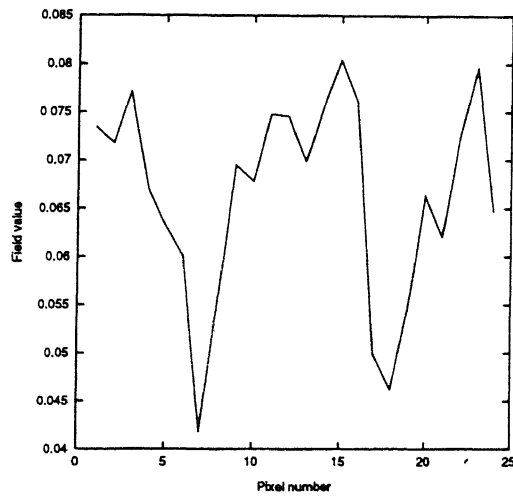


Figure 4.32: Line plot of the 6<sup>th</sup> row of the reconstructed field by 4 views

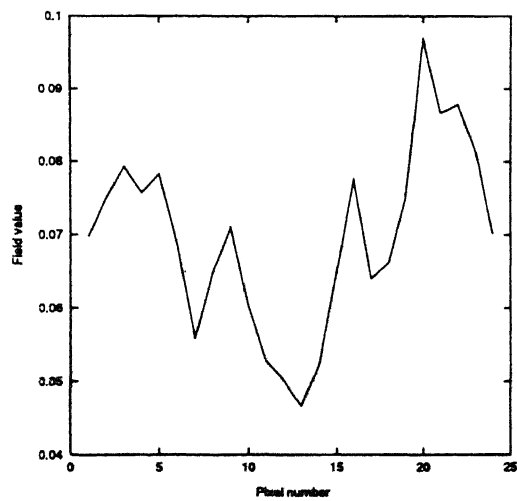


Figure 4.33: Line plot of the 12<sup>th</sup> row of the reconstructed field by 4 views

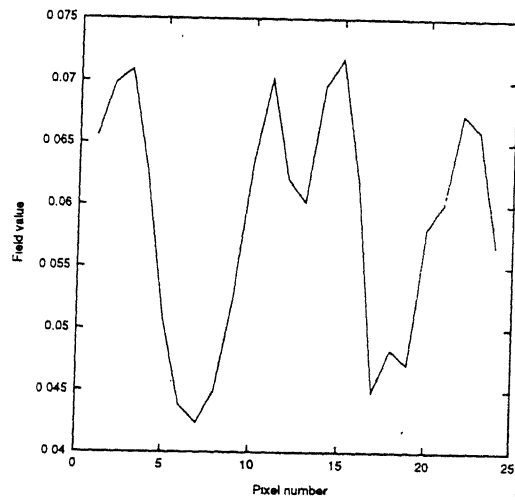


Figure 4.34: Line plot of the 18<sup>th</sup> row of the reconstructed field by 4 views

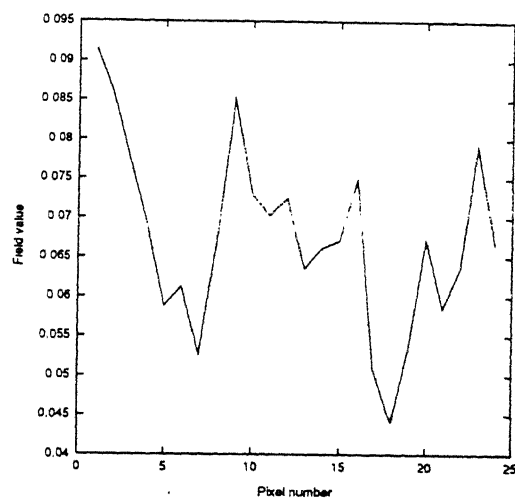


Figure 4.35: Line plot of the 6<sup>th</sup> row of the reconstructed field by 12 views

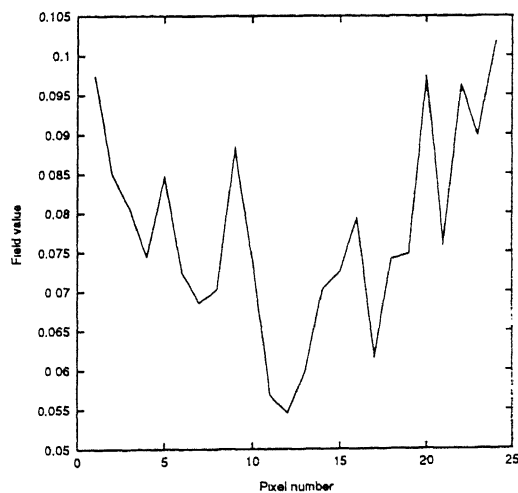


Figure 4.36: Line plot of the 12<sup>th</sup> row of the reconstructed field by 12 views

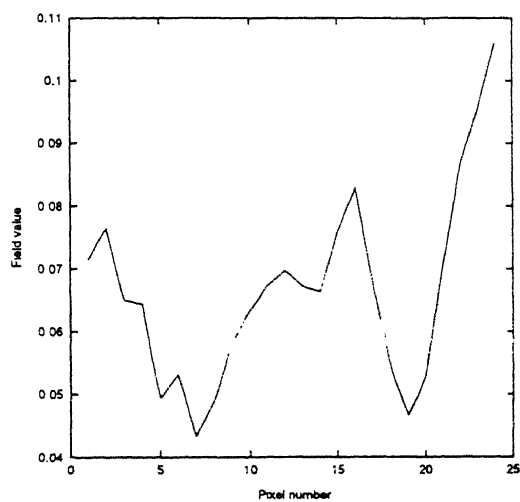


Figure 4.37: Line plot of the 18<sup>th</sup> row of the reconstructed field by 12 views

# Chapter 5

## Results

In this chapter the performance of algorithms on simulated and real data is discussed.

### 5.1 Simulated data

#### 5.1.1 Performance of ART

Table 4.2 compares the performance of ART family. Mayinger ART requires fewer iterations to converge but errors in reconstructed field are higher among all the ARTs. Whereas, Gilbert ART takes higher CPU time to converge but the errors introduced in reconstructed field are lower. Gordon and Anderson ARTs show nearly same performance.

#### 5.1.2 Performance of MART

Table 4.3 compares the performance of MART family. GBH does not converge at higher value of relaxation parameter. Among the four MARTs, Lent2 is the best. It requires fewer iterations to converge and errors in the field predicted by Lent2 is lower.

GBH converges only for lower values of relaxation factor. It was tested for the relaxation factor of 0.01 and it produces oscillations during iterative process. It converged sharply to a value of about 0.7 within iterations about 40 and again diverged. It shows the convergence behaviour again after iterations of about 3000. GBH converged to 0.01 at very low value of relaxation parameter of 0.0001 but requires a large number of iterations and the errors in the reconstructed field is maximum as compared to other MARTs.

### 5.1.3 Effect of relaxation parameter on ART and MART

Variation of errors and iterations with relaxation factor is shown in Tables 4.5 and 4.6 for Gilbert ART and Lent2, respectively. In Gilbert ART, as the value of relaxation factor is increased from 0.01 to 1.99, the iterations decrease but errors first decrease and then increase sharply. 0.5 may be taken as the optimal value of relaxation factor for Gilbert ART. In Lent2, as the relaxation factor is increased from 0.01 to 1.99, the convergence time first reduces, become minimum at relaxation factor of 1.0 and then increases. Same is true with errors. Hence, for Lent2, best value of relaxation parameter is 1.0.

### 5.1.4 Comparison between ART and MART

Among the eight algorithms, MARTs are most accurate as compared to ARTs, although ARTs converge at lower iterations. Figures from 4.3 to 4.14 also verify the better performance of MART over ART. Lent2 is superior among all, it reconstruct the field with lowest errors. The ability to determine 2500 unknowns, with lower errors, from the set of 312 equations, shows the strength of Lent2.

*Gilbert ART* and *Lent2* is further tested on CosGauss phantom for the 9 sets of projection data. Results are reported in Tables 4.7 to 4.10.

- As the number of projections increase the error reduce, though convergence time increases. This is true, since more and more information is

now added or in simple words, more number of projections means more number of equations to solve 2500 unknowns.

- Increasing the viewing angle decreases the errors. As tables 4.8 and 4.10 predict that the field reconstructed by the data sets of viewing angle  $90^\circ$  is more erroneous than the field reconstructed by the data set of viewing angle  $180^\circ$ .
- Orthogonality in the data sets also give the unique results. As seen from case E, which contains two sets of orthogonal projections at  $(0^\circ, 90^\circ)$  and  $(45^\circ, 135^\circ)$ . Here data sets contains projections at 4 angles and total rays are only 240, but it shows better results as compared to cases C, D, F in the Gilbert ART, even though these cases contain more number of projections and rays. In Lent2, case E may not be considered superior to cases C, D, F but may be considered comparable with them.

Figures also show that case 5( $180^\circ$ ) is better than case 5( $90^\circ$ ) and case 18( $180^\circ$ ) reconstruct the field which seems to be replica of the exact field.

**Lent2** begin the superior among all the algorithms is further applied to the 4 simulated objects. These objects are reconstructed using three important projection sets, that are cases C, F, I.

The exact field and the reconstructed field are shown in the figures 4.15 to 4.28. All the contour plots have the same contour levels. The contour interval is always 0.2 units.

- **Reconstruction by case C:** Though it shows the location of holes or inclusions, but is not able to reconstruct them with exact shape and size. The circular holes take the form of ellipse. This is true, since the object is scanned from  $0^\circ$  to  $90^\circ$ . Plots of figures 4.19 to 4.21 also show the poor reconstruction of holes. The exact absorption coefficient of holes is 0 but the reconstructed value comes nearly 0.2, also the absorption coefficient of plate reduces to about 0.7.
- **Reconstruction by case F:** Reconstruction improves as compared to case C. Still holes with exact shape and size are not reconstructed. Line

CENTRAL LIBRARY  
1.1.1.1  
125020  
A



plots show the absorption coefficient of reconstructed holes and plate is about 0.2 and 1.2, respectively. Holes, although do not become perfectly circular but their shape improves as compared with case C. This also supports the argument that increasing the angle of view decreases the error levels.

- **Reconstructed by case I:** This case gives surprisingly good results. Reconstructed field resembles the exact field. Line plots also show that plate and holes are reconstructed with absorption coefficient 1 and 0 respectively, except at the edges, where, a small error is present. These reconstructions also prove that larger are the number of projections, more accurate is the reconstruction.

All the cases are able to predict the presence of *inclusions* in the plate. Although, reconstructions by cases C and F are not exact. Case I predict the exact location, shape and size of inclusions. This study shows the ability of algorithm to notice a small change in field values.

Non-symmetrical case, i.e square with two holes, is also perfectly reconstructed. This result shows that the algorithm can be applied to any symmetrical or non-symmetrical cases.

If the field values are widely separated, i.e. the case in which absorption coefficient of holes is 10 and of plate is 100, algorithm is able to reconstruct the field. Here also, reconstruction by 5(180°) is better than 5(90°) and the reconstruction by 18(180°) is the best. Increasing the field values increases the error levels.

## 5.2 Experimental data

Field is reconstructed using 3 cases, which include reconstruction by 2 views, reconstruction by 4 views and reconstruction by 12 views. Figures 4.29 to 4.31 show the reconstruction for all the cases.

- **Reconstruction by 2 views:** Reconstructed field is shown in contour plot of figure 4.29. This plot consists of a number of contours at same level. Although, it consists of contours at five locations of holes, but due to presence of other contours, this reconstruction may not be considered as perfect.
- **Reconstruction by 4 views:** The reconstructed field consists of five holes, which can be clearly seen from the contour plot of figure 4.30. Plot shows the contours at the five hole locations. This result shows the uniqueness of orthogonal projections. The two sets of orthogonal projections, i.e.  $(0^\circ, 90^\circ)$  and  $(45^\circ, 135^\circ)$ , are able to reconstruct the field with very low errors. The ability of algorithm to determine 576 unknown (pixel values) from the set of 116 equations (number of rays) using data sets which include projections at 4 angles  $(0^\circ, 45^\circ, 90^\circ, 135^\circ)$  is really surprising and the importance of this set of angles is evident.
- **Reconstruction by 12 views:** Increasing the number of views must improve the reconstruction but here reconstructed field distorts. Holes become broad and take arbitrary shapes. It seems that, beside adding more informations, noise is indirectly added. Broadening of holes is due to shift in the information, i.e., reconstruction of a part by the information of some other part. This may be true if the lateral displacement of object by some distance, say  $x$ , does not move it exactly by that distance or due to improper rotation. Reconstructed field is shown in figure 4.31.

Line plots of  $6^{th}$ ,  $12^{th}$  and  $18^{th}$  rows of the reconstructed field by 4 views and 12 views are shown in figures 4.32 to 4.37. These figures, also indicate the broadening of holes. Broadening of holes in the field reconstructed by 12 views is more than in the field reconstructed by 4 views.

# Chapter 6

## Conclusions

In this study, four different MART algorithms and four different ART algorithms were programmed. These algorithms were compared with respect to their performance on CosGauss phantom, a numerically generated object. The following conclusions are drawn:

1. Of the all algorithms tested, Lent2 gives best results in term of reconstruction accuracy.
2. Among ART, Gilbert ART performs better, however its performance is poor when compared to MART.
3. Relaxation parameter of 0.5 for Gilbert ART and 1.0 for Lent2 gives reasonably good results in terms of CPU time and errors.
4. All the algorithms show a systematic behaviour with respect to the number of projections and view angles. Increasing the number of projections decreases the errors in the reconstructed field but increases the CPU time.
5. Increasing the angle of view decreases the error levels in the reconstructed field.
6. Reconstruction improves when at least two projections are orthogonal to each other.

7. Inclusions present in the solid objects can be predicted reasonably well.
8. Algorithms may be applied to any symmetrical or non-symmetrical objects.

**Experimental results** shows that, Lent2 produces superisingly good reconstruction from limited amount of data, even when the data has a significant amount of noise. The data set includes projections at 4 angles over a  $180^\circ$  total angle of view ( $0^\circ$ ,  $45^\circ$ ,  $90^\circ$ ,  $135^\circ$ ). The uniqueness of this set of angles, i.e. two sets of orthogonal angles, is evident from this result.

## 6.1 Suggestions for future work

1. Dependence of the reconstructed field on the initial approximation of the field may be studied.
2. The algorithms may be further tested on the numerically generated data with added noise.
3. These algorithms may be applied to the ultrasonic TOF data, to test their performance on the non-linear data.
4.  $\gamma$ -ray CT scanner may be used to scan composite materials to study its ability to reconstruct the field of an object with varying absorption coefficient.
5. Other series expansion methods may also be studied.

# References

- [1] G. T. Herman, 1980, *Image reconstruction from projections: the fundamental of computerized tomography*, Academic Press, New York.
- [2] P. M. V. Subbarao, P. Munshi, K. Muralidhar, 1997, *Performance of iterative tomography algorithms applied to Non-destructive evaluation with limited data*, NDT&E International, vol 30, 359-370.
- [3] D. Datta, 1995, *A methodology in ultrasonic NDE for identification and reconstruction of defects in fibre composites*, Ph.d. thesis.
- [4] P. Munshi, 1990, *A review of computerized tomography with application to two-phase flows*, Sadhana, vol. 15, 43-55.
- [5] R. Gordon, R. Bender, G. T. Herman, 1970, *Algebraic reconstruction technique (ART) for three-dimensional microscopy and X-ray photography*, J. Theor. Biol., vol 29, 471-481.
- [6] M. S. Kaczmarz, 1937, *Angenaherte auflosung von systemen linearer gleichungen*, Bull. Acad. Polonaise Sci. Lett. Classe Sci. Math. Natur. Serier A35, 355-357.
- [7] G. N. Hounsfield, 1973, *Computerized transverse axial scanning tomography. Part I: Description of the system*, Br. J. Radiol, vol 46, 1016-1022.
- [8] Y. Censor, 1983, *Finite series-expansion reconstruction methods*, Proceedings of the IEEE, vol. 71, 409-419.
- [9] R. Gordon, 1974, *A tutorial on ART*, IEEE Transaction on nuclear science, vol. 21, 78-93.

- [10] F. Mayinger, 1994, *Optical measurements*, Springer-Verlag, New York.
- [11] P. F. C. Gilbert, 1972, *Iterative methods for three-dimensional reconstruction of an object from its projections*, J. Theo. Biol., vol 36, 105-117.
- [12] A. H. Anderson, A. C. Kak, 1984, *Simultaneous algebraic reconstruction technique (SART): a superior implementation of the ART algorithm*, Ultrason. Imaging, 6.
- [13] D. Verhoven, 1993, *Multiplicative algebraic computed tomographic algorithms for the reconstruction of multidirectional interferometric data*, Optical Engineering, vol 32, 410-419.
- [14] R. Gordon, G. T. Herman, 1974, *Three-dimensional reconstruction from projections: a review of algorithms*, Int. Rev. Cytol, vol 38, 111-151.
- [15] A. Lent, 1977, *A convergent algorithm for maximum entropy image reconstruction, with a medical X-ray application*, Proc. SPIE Image Analysis and Evaluation, R. Shaw, Ed., 249-257.



125020

## Date Slip

This book is to be returned on the  
date last stamped. 125020

This image shows a blank sheet of white paper with horizontal blue ruling lines. A single vertical red margin line runs down the left side of the page. The paper appears to be from a notebook or a standard writing template. There are no markings, text, or drawings on the page.

NETP-1997-M-VAR-EXP



A125020